공학박사학위논문

# Phosphorus-based High Capacity Negative Electrode Materials for Sodium-ion Batteries

인을 기반으로 하는 나트륨 이온 전지용

고용량 음극 활물질

2016년 2월

서울대학교 대학원

화학생물공학부

김 영 진

# Abstract

In recent years, the demand for large scale energy storage devices has increased with the development of electric vehicles (EVs) and energy storage system (ESS), and Li-ion batteries are considered promising candidates because of their high energy density. However, there is growing concern that lithium resources are insufficient to meet the demands of large scale applications due to the limited reserve and too geographically constrained. Actually, the recent price of lithium raw materials has shown sharp increases. Cosquently, Na-ion batteries are an alternative to Li-ion batteries because sodium resources are much more abundant and inexpensive than lithium. However, there is a critical obstacle to their development. The energy density of Na-ion batteries is slightly lower than that of Li-ion batteries because the reversible capacity and operating voltage of currently reported electrode materials in Na-ion batteries are lower in comparison. This implies that it is not easy to replace Li-ion batteries with Na-ion batteries because the cost per energy stored ($/Wh) of Na-ion batteries does not provide much advantage. Therefore, new negative electrode materials having higher reversible capacities are necessary if one is to increase the energy density of Na-ion batteries.

In this study, firstly, exploring the possibility and investigating electrochemical reaction mechanism of red phosphorus as negative electrode materials for sodium-ion battery are performed based on thermodynamic information. In order to improve electrical conductivity, carbon coating via ball-milling is carried out. This carbon coating is enhanced electrochemical reactivity including the highest specific capacity among any reported negative electrode materials. The understanding is that during the

sodiation process amorphous red phosphorus undergoes a phase change to crystalline sodium phosphide ($Na_3P$) by electrochemical reaction and structure analysis. The corresponding to $Na_3P$ peaks in dQ/dV plots are shown at the *ca.* 0.2 and 0.55 V *vs.* $Na/Na^+$ during sodiation and desodiation, respectively. However, poor cycle performance is observed due to volume change during charge/discharge.

Secondly, the study on failure mechanism and enhanced cycle performance of phosphorus electrode materials are carried out. The failure mechanism of this material comes from volume change. The large volume change of electrode materials is attributed to be the main reason for their rapid capacity loss. It increases internal resistance by contact loss between phosphorus and conducting agent. The instability of solid electrolyte interphase (SEI) at the electrode surface via repetitive volume expansion is also considered to failure mechanism. In order to improve cell performance, tried to change the phosphorus to carbon ratio and add electrolyte additive such as fluoroethylene carbonate (FEC). In case of increasing active materials, it is shown alleviating volume expansion. In addition, excellent cycle performance is observed for 100 cycles with FEC additives in electrolytes. It is attributed that NaF-like SEI film is mechanically strong and EC decomposition is minimized.

Finally, the volumetric capacity is improved by $Sn_4P_3$ electrode materials. Phosphorus has poor electrical conductivity. Accordingly, a large amount of carbon has to be used in order to enhance their electrical conductivity, leading to decreases their gravimetric and volumetric capacity. The volumetric capacity in a cell is one of the most key factors that determine its feasibility as a post battery. Therefore, it is important to develop new negative electrode materials delivering high volumetric capacity for sodium-ion batteries. $Sn_4P_3$ is one of the candidates for high volumetric

capacity electrode materials. $Sn_4P_3$ showed excellent electrochemical performance for Na-ion batteries. $Sn_4P_3$ delivered a high volumetric capacity and exhibited very stable cycle performance with a negligible capacity fading over 100 cycles. The redox potential of $Sn_4P_3$ is lower than that of phosphorus, indicating that the energy density of full cells with $Sn_4P_3$ can be higher than those of cells with phosphorus when the same reversible capacity is utilized.

# List of Figures

**List of Tables**

**Table 1.** The lattice parameters of $Sn_4P_3$ compounds obtained from Rietveld refinement.

# Contents

# 1. Introduction

In modern society, mankind requires more and more energy to improve our life, the lack of fossil fuel; environmental pollution and global warming have given rise to a serious inconsistency.[1,2] As a part of efforts to overcome these problems, many researchers are considering how to shift a new paradigm from fossil fuel based energy to renewable energy. These sustainable energies must need to energy storage devices.[3-5] Thanks to their excellent electrochemical performance, for several decades, Li-ion batteries have been successfully utilized as a power source in hybrid electric vehicles and mobile electronic devices such as mobile phones and lap-top computers. However, the present technology for Li-ion batteries is not expected to be able to meet the demands for power sources in future energy storage applications. In addition, lithium resources are expensive and too geographically constrained.[6,7] Accordingly, new rechargeable battery systems such as sodium ion, sodium metal, magnesium, metal-air, and metal-sulfur batteries are being considered as alternatives to replace Li-ion batteries. In particular, Na-ion batteries have attracted rapidly increasing attention owing not only to the low cost of sodium due to its abundant resources but also their better safety compared to sodium metal batteries such as high-temperature Na−S batteries.[8-15]

Because of their low cost, the main potential application of Na-ion batteries is considered to be large-scale energy storage systems (ESS). However, it should be stressed that it is not easy to decrease the cost of Na-ion batteries relative to that of Li-ion batteries, in spite of the inexpensive Na precursors. In particular, Na-ion batteries have slightly lower energy densities than Li-ion batteries, which means that the cost per energy ($/Wh) of Na-ion batteries cannot easily be decreased because the energy density limitations offset the cost savings due to the use of Na. Precursors for transition metals such as Co, Ni, and Mn are much more expensive than precursors for alkali metals such as Li and Na, and the cost of sodium carbonate is only about 10% of the total cost of the precursors for the positive electrode materials, although the cost of positive electrode materials is the dominant expense (36%) for these batteries. Thus, only a 3.6% cost reduction is expected to be possible by replacing positive electrode materials.[8]

However, unlike for Li-ion batteries, a cheap Al current collector can be used for the negative electrode in Na-ion batteries instead of an expensive Cu current collector, because Al does not alloy with Na. This can lead to a cost reduction of about 8%. A slight cost reduction is also expected to be gained by replacing Li salts with Na salts in the electrolytes. Therefore, Na-ion batteries

are considered to be potentially about 10% less expensive in total cost than commercialized Li-ion batteries, assuming they deliver the same energy density. However, most electrode materials that have been introduced for Na-ion batteries to date show similar or slightly lower specific capacities and redox potentials than those for Li-ion batteries, resulting in the lower energy density for the Na-ion batteries. This indicates that the cost reduction achieved by using Na-ion batteries may not be significant in terms of the cost per energy. Therefore, it is important to develop electrode materials with high energy densities for Na-ion batteries in order to reduce the cost per energy.

The energy density can be improved by i) using electrode materials with high specific capacities, ii) using positive electrode materials with high redox potentials, and iii) using negative electrode materials with low redox potentials. However, most positive electrode materials store Na ions via intercalation chemistry, which means that the number of storage sites is limited. This suggests that it will be difficult to greatly increase the specific capacity of the positive electrode materials. The use of positive electrode materials with high redox potentials is also limited because of electrolyte decomposition at high potentials. Most commercialized electrolytes even for Li-ion batteries are unstable and decompose at over 4.8 V $vs.$ Li/Li$^+$. Therefore, the best approach is

developing negative electrode materials with high specific capacities and appropriately low redox potentials in order to improve the energy density of Na-ion batteries so that they can successfully replace Li-ion batteries. This reveals that a similar energy density to those of commercialized Li-ion batteries (150-200 Wh kg$^{-1}$, 400-650 Wh L$^{-1}$) can be achieved by using only high-capacity negative electrode materials.

Therefore, in this study, focus on the development of the high capacity negative electrode materials. First, the use of red phosphorus with carbon composites based on Na-P binary phase diagram as active materials for sodium-ion battery is practiced. In addition, failure mechanism of this composites and optimization of cell performance are studied by change the phosphorus to carbon ratio and electrolyte additives. This composite shows reversible capacity over 1000 mA h g$^{-1}$, appropriate redox potential of *ca.* 0.4 V *vs.* Na/Na$^+$, and excellent cycle performance with negligible capacity fading over 100 cycles. This specific capacity of the composite is the highest value among Na-ion insertion materials reported to date. Second, this work demonstrates that high volumetric capacity negative electrode materials are realized with intermetallic compound such as tin phosphide (Sn$_4$P$_3$). As above mentioned, red phosphorus must be performed carbon coating in order to use active materials due to very

low electric conductivity. This P/C composites gives arise to decreasing volumetric capacity. Therefore, in order to increase the volumetric capacity, intermetallic compound between phosphorus and tin is used negative electrode materials for sodium-ion battery. Also, electrochemical reaction mechanism is investigated by *ex-situ* TEM, XRD, and EXAFS.

# 2. Background

## 2.1. Sodium-ion batteries

Thanks to their excellent electrochemical performance, for several decades, Li-ion batteries have been successfully utilized as a power source in hybrid electric vehicles and mobile electronic devices such as mobile phones and lap-top computers.[1,2] However, the present technology for Li-ion batteries is not expected to be able to meet the demands for power sources in future energy storage applications. In addition, lithium resources are expensive and too geographically constrained.[6,7] Accordingly, new rechargeable battery systems such as sodium ion, sodium metal, magnesium, metal-air, and metal-sulfur batteries are being considered as alternatives to replace Li-ion batteries. In particular, Na-ion batteries have attracted rapidly increasing attention owing not only to the low cost of sodium due to its abundant resources but also their better safety compared to sodium metal batteries such as high-temperature Na−S batteries.[8-15]

Because of their low cost, the main potential application of Na-ion batteries is considered to be large-scale energy storage systems (ESS). However, it should be stressed that it is not easy to decrease the cost of Na-ion batteries relative to

that of Li-ion batteries, in spite of the inexpensive Na precursors. In particular, Na-ion batteries have slightly lower energy densities than Li-ion batteries, which means that the cost per energy ($/Wh) of Na-ion batteries cannot easily be decreased because the energy density limitations offset the cost savings due to the use of Na. **Figure 1** shows the cost of each part of the cell in a Na-ion battery. Precursors for transition metals such as Co, Ni, and Mn are much more expensive than precursors for alkali metals such as Li and Na, and the cost of sodium carbonate is only about 10% of the total cost of the precursors for the cathode materials, although the cost of cathode materials is the dominant expense (36%) for these batteries. Thus, only a 3.6% cost reduction is expected to be possible by replacing cathode materials. However, unlike for Li-ion batteries, a cheap Al current collector can be used for the anode in Na-ion batteries instead of an expensive Cu current collector, because Al does not alloy with Na. This can lead to a cost reduction of about 8%. A slight cost reduction is also expected to be gained by replacing Li salts with Na salts in the electrolytes. Therefore, Na-ion batteries are considered to be potentially about 10% less expensive in total cost than commercialized Li-ion batteries, assuming they deliver the same energy density. However, most electrode materials that have been introduced for Na-ion batteries to date show similar or slightly lower specific capacities and redox potentials than those for Li-ion batteries, resulting

in the lower energy density for the Na-ion batteries. This indicates that the cost reduction achieved by using Na-ion batteries may not be significant in terms of the cost per energy. Therefore, it is important to develop electrode materials with high energy densities for Na-ion batteries in order to reduce the cost per energy.

The energy density can be improved by i) using electrode materials with high specific capacities, ii) using cathode materials with high redox potentials, and iii) using anode materials with low redox potentials. However, most cathode materials store $Na^+$ ions via intercalation chemistry, which means that the number of storage sites is limited. This suggests that it will be difficult to greatly increase the specific capacity of the cathode materials. The use of cathode materials with high redox potentials is also limited because of electrolyte decomposition at high potentials. Most commercialized electrolytes even for Li-ion batteries are unstable and decompose at over 4.8 V *vs.* $Li/Li^+$. Therefore, the best approach is developing anode materials with high specific capacities and appropriately low redox potentials in order to improve the energy density of Na-ion batteries so that they can successfully replace Li-ion batteries.
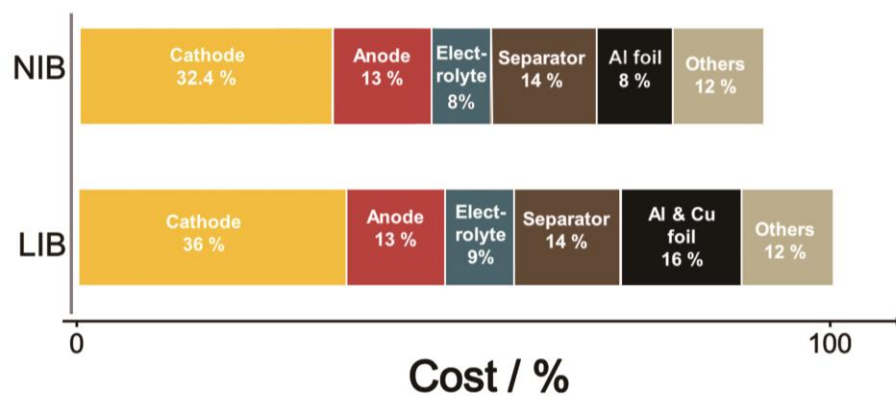
**Figure 1** Comparison of the manufacturing costs for Li-ion batteries (LIB) and Na-ion batteries (NIB).

## 2.2. Negative electrode materials

### 2.2.1. Carboneous materials

Owing to its relatively high specific capacity, stable cycle performance, and low redox potential similar to Li, graphite has been the most commonly used to Li-ion batteries negative electrode material was commercialized by Sony since 1991. Carbon is well known for formation of many allotropes due to its valency. Well-known forms of carbon are graphite and diamond. In recent decades many more allotropes have been reported and researched such as graphene, buckminsterfullerene, and carbon nanotubes and so on. Of these, graphite is one of the most representative allotropes of carbon. This structure is the *P63/mmc* space group of the hexagonal crystal system. The graphene layers are stacked together in graphite. The graphite is able to be intercalated one Li atom per six carbon ring with a theoretical specific capacity of 372 mA h $g^{-1}$. Unfortunately, unlike the successfully commercial application for negative electrode material of graphite in LIBs, the sodium intercalation into graphite is not favorable. It has been studying various C–Li binary phases, whereas that of C–Na is not available. Also, sodiation of graphite has not been reported in carbonate based electrolyte.[16,17] Recently, insertion of Na into graphite is reported using ether

based electrolyte. It indicates that the insertion of Na ions into graphite materials is thermodynamically unfavorable process. It is different to voltage profiles between insertion and extraction of Li and Na in graphite electrode, respectively. The Li ions are reversible inserted and de-inserted into graphite in lithium–ion battery. However, graphite as negative electrode materials for sodium-ion battery showed irreversible sodiation.

In alternate carboneous negative electrode materials of the sodium-ion battery include a hard carbon that is capable of insertion sodium ions. Hard carbon has been studied due to much more advantage than graphite in lithium-ion battery. It is high capacity, no intercalation-induced exfoliation, fast rate capability, easy to form composites, and molecularly doped negative electrode materials. The hard carbon in NIBs delivered specific capacity of near 300 mA h g$^{-1}$ close to that of graphite in LIBs.[18-20] The voltage profiles of hard carbon are shown in sloping and low-potential plateau. Most of the sodium ions are inserted in nano-porous voids in hard carbon; another is interacted in a misaligned graphene layer.

### 2.2.2. Alloy-based materials

Alloy materials such as Si, Ge, Sn, and Sb have been widely examined for Li-ion battery applications because their specific capacities are higher than those of commercialized carbonaceous materials such as graphite. As is the case for Li-ion batteries, alloy materials are considered promising anode materials for Na-ion batteries owing to their high specific capacities, as shown in **Figure 2**. Si and Sn have attracted more attention than Ge and Sb in Li-ion batteries because of the better electrochemical performance of Si and Sn including their higher specific capacities and lower redox potentials. In addition, Ge and Sb are more expensive than Si and Sn. Furthermore, a lower redox potential of anode materials is beneficial for achieving higher energy densities of full cells, and thus Si and Sn have been considered more promising than Ge and Sb. However, for Na-ion batteries, the redox potentials of Si and Sn are too close to that of Na metal, because the redox potential of Na metal is higher than that of Li metal by 0.3 V. In the other words, while the redox potentials of Si and Sn are appropriate for Li-ion batteries, their redox potentials are close to 0 V *vs.* Na/Na$^+$, which is detrimental to Na-ion batteries because even a small amount of polarization imposes kinetic limitations on electrochemical insertion of Na

ions, resulting in abrupt capacity fading. Moreover, no report has experimentally shown the electrochemical sodiation of Si-based materials yet, although it is known that Si can theoretically alloyed with Na to form a NaSi phase.[21] Therefore, Sb and Ge have been considered more promising anode materials than Sn and Si for Na-ion batteries.
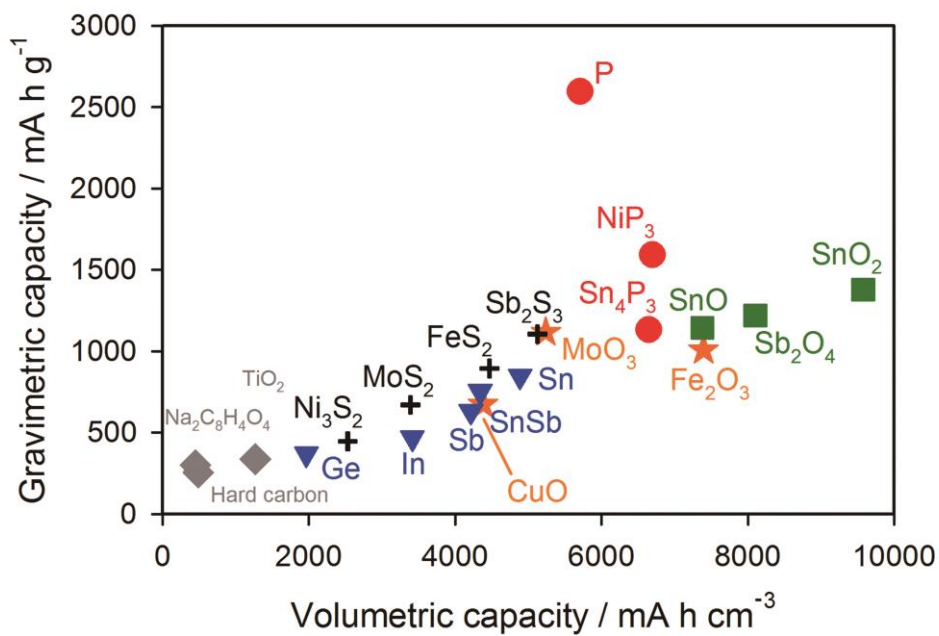
**Figure 2** Theoretical gravimetric and volumetric specific capacities of various negative electrode materials for Na-ion batteries.

### 2.2.3 Conversion reaction

In spite of the commercial success, the limited capacity of 372 mA h g$^{-1}$ for graphite is a difficult problem to slove. In 2000, Tarascon *et al.* reported reversible electrochemical performance of late 3d transition metal oxides including CoO, NiO, and FeO so-called conversion reaction as negatve electrode materials for LIBs.[22] The general insertion and conversion reaction can be written as equation (1) and (2), respectively.

$$M_aX_b + Li^+ + e \rightleftarrows LiM_aX_b \qquad (1)$$

$$M_aX_b + (bc)\,Li^+ + e \rightleftarrows aM + bLi_cX \qquad (2)$$
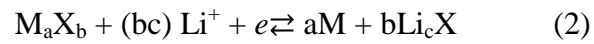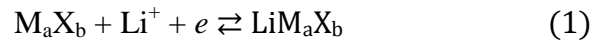
M is a transition metal and X is a non-metal (i.e. O, P, F, N, S, H and so on), respectively. The specific capacity of conversion reaction delivers over two times compared to insertion mechanism. Full reduction of the transition metal during lithiation leads to higher capacities compared to graphite. Also, excellent cycle performance is observed because nano-sized transition metal is dispersed in Li$_2$O matrix during lithiation.

Recently, it has been reporting to conversion reaction for sodium-ion battery to increase specific capacity. However, it is reported that its specific is lower than LIB and nitride is hard to work thermodynamically due to positive Gibbs free energy of $Na_3N$. Therefore, in order to increase capacity and improve reversibility of conversion reaction, need to further study based on reaction between non-metal and sodium.

# 3. Experimental

## 3.1. Simulation method

Ab-initio calculations were performed using density functional theory (DFT) with the spin-polarized generalized gradient approximation (GGA) and the Perdew-Burke-Ernzerhof functional for the exchange correlation. We used the projector augmented wave (PAW) method with a plane wave basis set as implemented in Vienna ab-inito simulation package (VASP). A plane-wave basis with an energy cutoff of 400 eV was used and appropriate numbers of k-points were used, depending on the size of the unit cells. All geometric relaxations were performed until all forces of the system converged within 0.05 eV/Å . The kinetic of 500 eV and reciprocal-space k-point meshes of $4 \times 4 \times 4$ using the Monkhorst-Pack scheme were included in all calculation. For ab initio molecular dynamics simulation, the k-point was only sampled at the gamma point. All geometric relaxations were performed until all forces of the system converged within 0.01 eV/Å . The calculated voltage upon sodiation is calculated by the standard approach.

## 3.2. Synthesis of active materials

### 3.2.1. Phosphorus and graphite composites

Amorphous red phosphorus/graphite composite was prepared via a mechanical ball milling using red phosphorus powder (Sigma Aldrich) and natural graphite (Alfa aesar) under an Ar atmosphere for 20 hours. The weight ratio of graphite : red P was 1:9, 7: 3, and 5:5 (weight ratio), respectively.

### 3.2.2 Tin phosphide

$Sn_4P_3$ powder was prepared via mechanical ball milling using Sn (Aldrich, $\geq$ 99%) and red phosphorus powders (Aldrich, $\geq$ 99.99%). The molar ratio of Sn and P powders was 4:3. High energy mechanical ball milling was carried out under an Ar atmosphere for an hour.

## 3.3. Electrochemical characterization

Samples of active materials were mixed with carbon black (Super P) and polyacrylic acid (PAA) in a 7:1:2 weight ratio. The slurry was cast onto current

collector (Cu). The electrodes were dried at 120 $^{\circ}$C in a vacuum oven overnight. Their electrochemical characteristics were evaluated using 2032 coin cells with a Na metal anode and 1 M sodium perchlorate (NaClO$_4$, Aldrich, $\geq$ 98 %) in an ethylene carbonate and diethyl carbonate (1:1 v/v, PANAX ETEC Co., Ltd., Korea) electrolyte solution to which 5 wt.% fluoroethylene carbonate (FEC, Soulbrain Co. Ltd.) was added. A microporous polyolefin film was used as a separator. Galvanostatic experiments were carried out between 0.0 and 1.5 V (*vs.* Na/Na$^+$) at a current density of 100 or 200 mA g$^{-1}$ by using WBCS 3000 (WonATech, Korea) under room temperature.

## 3.4. Spectroscopic analysis

### 3.4.1. Surface analysis

To investigate the composition of F 1s on the electrode surface, the XPS experiments were carried out in an ultra-high vacuum (UHV) multipurpose surface analysis system (Sigma probe, Thermo) operating at a base pressure of $< 10^{-10}$ mbar. The photoelectrons were excited by an Al K$\alpha$ (1486.6 eV) radiation at a constant power of 150 W (15 kV and 10 mA). Attenuated Total Reflectance-Fourier transform infrared spectroscopy (ATR-FTIR) was

investigated

### 3.4.2. Structural analysis

Powder X-Ray diffraction (XRD) data were collected on a Rigaku D/MAX2500V/PC powder diffractometer using Cu-Kα radiation ($\lambda$ = 1.5405 Å) operated in the 2θ range of $10-80^{\circ}$. Extended X-ray absorption fine structure (EXAFS) data were obtained at the Pohang light source (PLS) with a ring current of 100 mA at 3 GeV. Data were collected in a transmission mode using gas-filled ionization chambers as detectors. A Si (1 1 1) monochromator crystal, subjected to detuning to 80% in intensity, was used to eliminate high-order harmonics.

### 3.4.3 Morphology analysis

SEM samples were examined using a JEOL JSM-6700F field-emission scanning electron microscope (FE-SEM). High-resolution TEM samples were investigated using a scanning transmission electron microscope (HR-TEM, STEM, JEOL JEM-2100F).

# 4. Results and discussion

## 4.1. The red phosphorus and carbon composites as high capacity negative electrode materials for sodium-ion battery and its electrochemical reaction mechanism

Over the past tens of years, the major energy source has been fossil fuels which are non-renewable, finite, and environmentally harmful. As a part of efforts to address these problems, Li ion batteries have been extensively studied to obtain more efficient energy storage systems.[23,24] However, the commonly used electrode materials in Li ion batteries are inorganic compounds of $LiCoO_2$, $LiFePO_4$, $LiMn_2O_4$ and $Li_4Ti_5O_{12}$ prepared from limited Li-containing mineral resources. This problem will be exacerbated if the demand for lithium, and hence its price, increases greatly as a result of widespread commercialization of electric vehicles. Accordingly, sodium ion batteries are an attractive alternative to replace lithium ion batteries because Na resources are inexhaustible and of lower cost.[8-10] Although, Na ion batteries have recently received a great deal of attention as a next generation system and have shown promising electrochemical performance including stable cycleability and good rate capability, they face the critical problem of lower energy density than Li ion batteries.[13-15] Most cathode and anode materials that have been introduced to

date for Na ion batteries show similar or slightly lower specific capacity and redox potential than those of Li ion batteries. In general, conventional cathode materials having a high redox potential have been developed based on intercalation chemistry, and it is thus difficult to highly increase the specific capacity of these cathode materials due to limited storage sites and oxidation state. Therefore, in order to improve the energy density of Na ion batteries, new anode materials having a high specific capacity and appropriately low redox potential should be introduced. Thus far, however, there have been few studies on sodium insertion materials for anodes with high capacity.[19,20,25-29] The general strategy for storing a large number of ions is to use conversion chemistry such as alloying materials. The representative example is Si-based materials, and Si can store 4.4 $Li^+$ ions per Si, delivering 4200 mA h $g^{-1}$. However, it is known that Na ions are not electrochemically inserted in Si, despite of the existence of Na-Si alloys. Accordingly, Si-based materials unfortunately cannot be used as anodes in Na ion batteries, although Si is the most promising anode material for Li ion batteries. Sn and Sb-based materials have meanwhile been introduced as promising anode materials having a high reversible capacity, but their specific capacities do not exceed *ca.* 1000 mA h $g^{-1}$.[30-32] In this study, we introduce, for the first time, an amorphous red P/carbon composite as an anode material for Na ion batteries. This composite shows

reversible capacity of 1890 mA h $g^{-1}$, appropriate redox potential of ca. 0.4 V *vs.* Na/Na$^+$, good rate capability delivering 1540 mA h $g^{-1}$ at a current density of 2.86 A $g^{-1}$, and excellent cycle performance with negligible capacity fading over 30 cycles. This specific capacity of the composite is the highest value among Na-ion insertion materials reported to date.

In 2007[33] and 2012,[34-37] crystalline black and amorphous black phosphorus were introduced as anode materials in lithium ion batteries, respectively, and they showed substantially improved reversibility relative to red phosphorus. However, black phosphorus is formed under high pressure, and this synthesis is not facile. Red phosphorus, on the other hand, is commercially available with ease, but it was reported that Li ions are irreversibly inserted in red phosphorus, and the deinsertion reaction is not reversible. However, Marino *et al.*[38] recently showed the reversible de/insertion of Li ions to crystalline red phosphorus via the preparation of a red phosphorus/mesoporous carbon composite by vaporization and condensation, although the composite showed poor Coulombic efficiency (less than 50%) and cycle performance. Inspired by the reversible de/insertion of crystalline red phosphorus for Li ions, we have demonstrated the electrochemical performance of amorphous red phosphorus as an anode material for Na ion batteries. I also suggest that the electrochemical

performance of amorphous red phosphorus is strongly dependent on the electrical conductivity and the volume change during sodiation and desodiation. To estimate average electrode potential in sodium-ion battery prior to experimental, the electrode potential as a function of Na insertion content in a material is calculated as

$$V = \frac{G_{Na_yM} - G_{Na_xM}}{y-x} - G(Na_{metal})$$ (3)

where G is the Gibbs free energy. Thus, the voltage profile represents the stable phases in the $Na_xM$ system, as the plateaus in the potential vs. Na contents related with phase transitions.[21,39,40] **Figure 3** shows the electrode potential during sodiation obtained by the DFT calculation of Na-P systems. The prediction of average potential was carried out using known crystal structures obtained from the Inorganic Crystal Structure Database (ICSD). Based on the thermodynamic structural characters, the calculation gives three plateaus for $Na_xP$, 1.14, 0.64 and 0.2 V (*vs.* $Na/Na^+$), which corresponds to the two-phase reaction of $Na_3P_{11}$, NaP and $Na_3P$, respectively. Its theoretical specific capacity is 2596 mA h $g^{-1}$, which are the most sodiated alloys ($Na_3P$) in the phase diagrams. However, the electrical conductivity of red phosphorus is below $10^{-14}$ S $cm^{-1}$.[41] Because the electrochemical reaction is reacted both ion and electron,
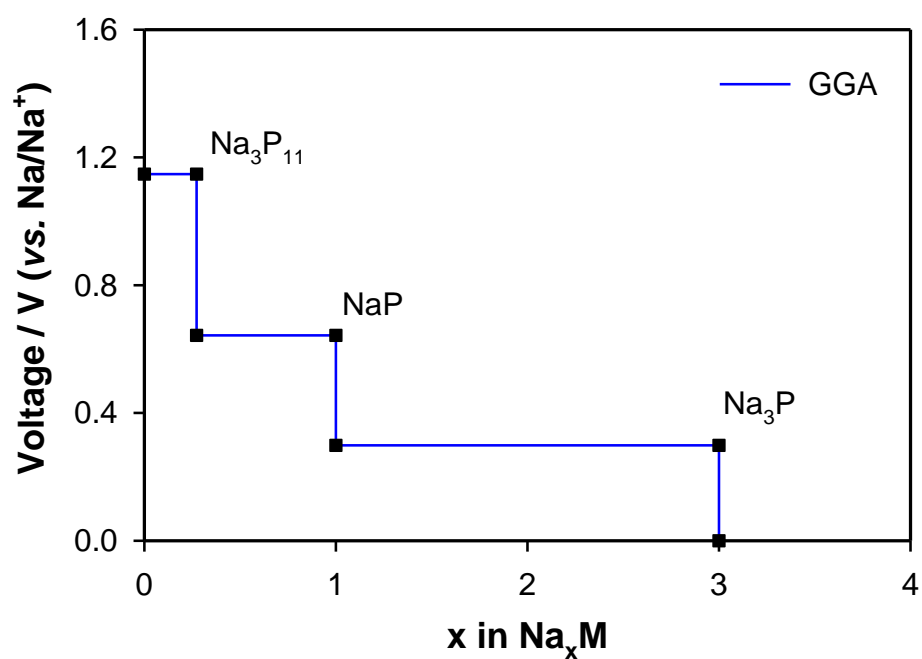
**Figure 3** Calculated electrode potential profiles for $Na_xP$ phases via known Na-M crystal structures.

electrical conductivity is improved.

The amorphous red phosphorus/carbon composite powders were obtained via a facile and simple ball milling process using commercially available amorphous red phosphorus and natural graphite carbon with a weight ratio of 9:1. The graphite to phosphorus weight ratio is denoted by GPxy (ration of graphite(x) and phosphorus(y)). The XRD pattern of **Figure 4a** shows that the resulting product is an amorphous red phosphorus/carbon composite, which is in agreement with previously reported amorphous red phosphorus. It was previously reported that amorphous red phosphorus is transformed into orthorhombic black phosphorus due to high temperature and pressure when a high energy mechanical milling (HEMM) technique is adopted.[33,34] However, the amorphous structure of red phosphorus was sustained in the composite due to the application of moderate temperature and pressure, because the conventional ball milling technique was utilized for the preparation of this phosphorus/carbon composite. This is further supported by the Raman spectra as shown in **Figure 4b**. The amorphous red phosphorus/carbon composite showed no Raman peak for phosphorus and only carbon peaks were observed at 1350 and 1580 cm$^{-1}$ for D- and G-bands, respectively. This seems to be attributed to that carbon is covered on phosphorus in the composite, resulting in
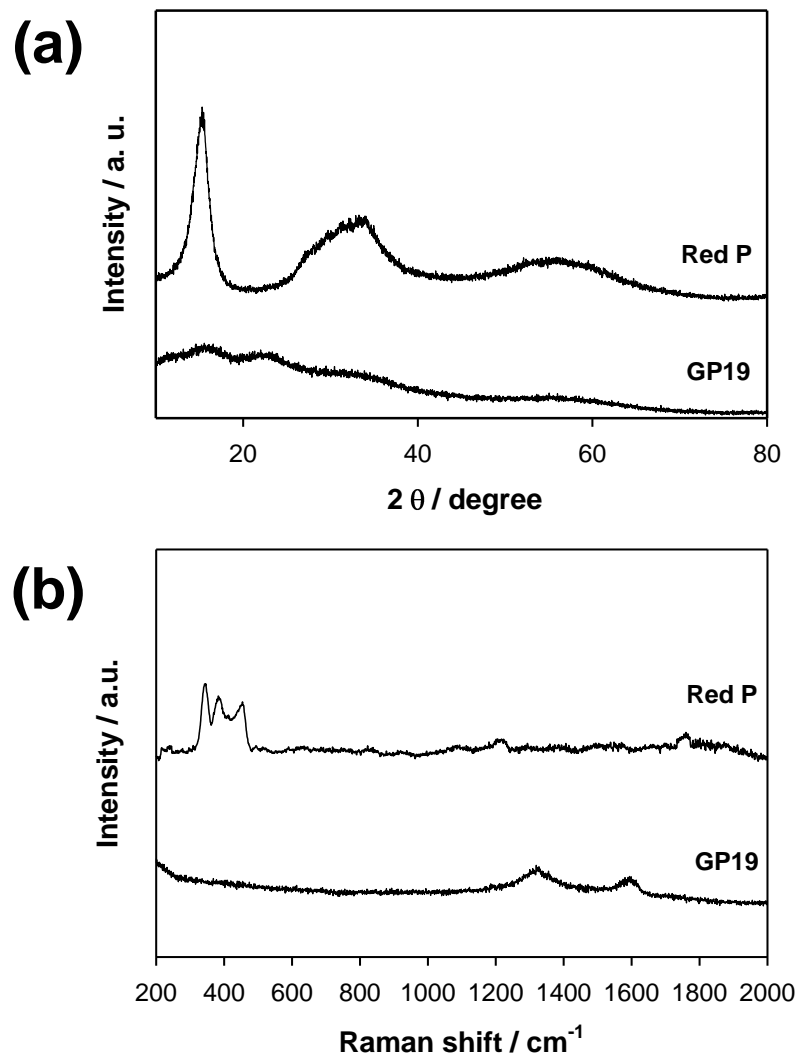
**Figure 4** (a) XRD patterns of bare red P and GP19. (b) Raman spectra of bare red P

decreasing the intensity of phosphorus peaks. Thus, the bare red phosphorus was ball-milled without carbon, and this shows the similar Raman spectrum of bare amorphous red phosphorus, which is different from that of black phosphorous.[34,42] TEM and EDS mapping images of the amorphous red phosphorus/carbon composite indicate that the thickness of its coating layer is below 10 nm (**Figure 5a**) and phosphorus and carbon are homogeneously mixed together on a nanoscale (**Figure 5b**), resulting in improved electrical conductivity. The electrical conductivity of the GP19 were $7.5 \times 10^{-7}$ S cm$^{-1}$, measured by the Van der Pauw method.[43] The electrical conductivity of the bare amorphous red phosphorus is known to be lower than $1 \times 10^{-14}$ S cm$^{-1}$. [32,44,45]The GP powders have a broad size distribution from hundreds of nanometers to a few micrometers, as shown in the FE-SEM images (**Figure 6**).

The electrochemical performance of the GP 19 was evaluated using a half cell with a sodium metal. Figure 5 shows the galvanostatic charge-discharge profiles of the composite electrode between 1.5 and 0 V at a current density of 200 mA g$_P^{-1}$. The sodiation profile is comprised of three regions located at ca. 1.2–0.5, 0.5–0.25 and 0.25 V *vs.* Na/Na$^+$ (two sloping regions and one plateau, respectively). The GP19 electrode delivered reversible capacity of 1490 mA h g$^{-1}$. The theoretical specific capacity of phosphorus is 2596 mA h g$^{-1}$, assuming Na$_3$P is formed, and thus, the amorphous red phosphorus/carbon composite
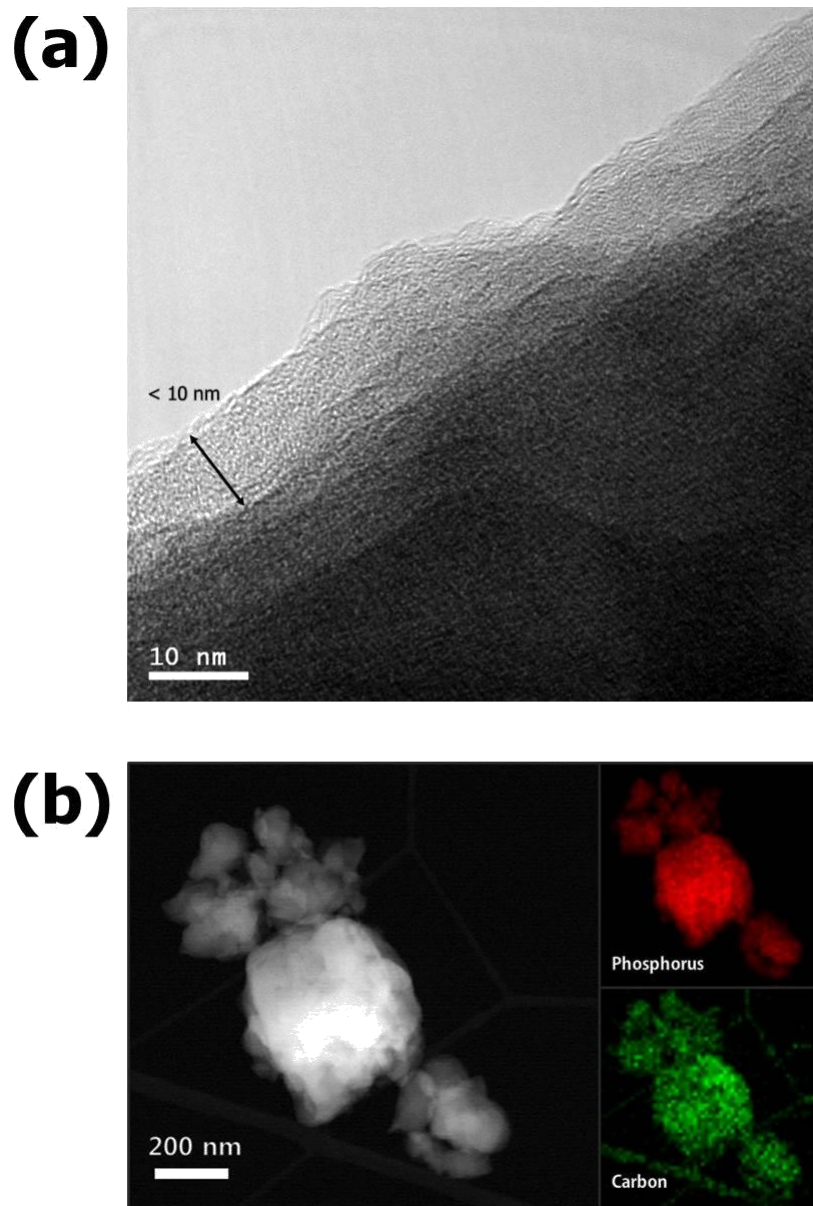
**Figure 5** (a) HR-TEM image of GP19. (b) TEM image of amorphous red P/C composite and the corresponding EDS mapping images of phosphorus and carbon.
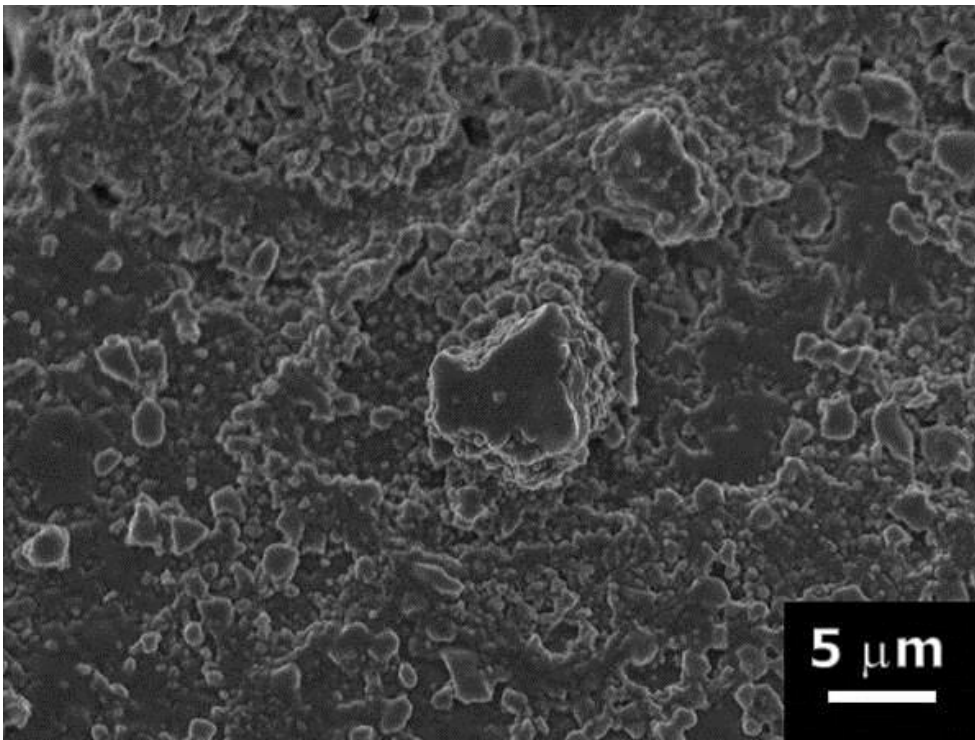
**Figure 6** FE-SEM image of GP19
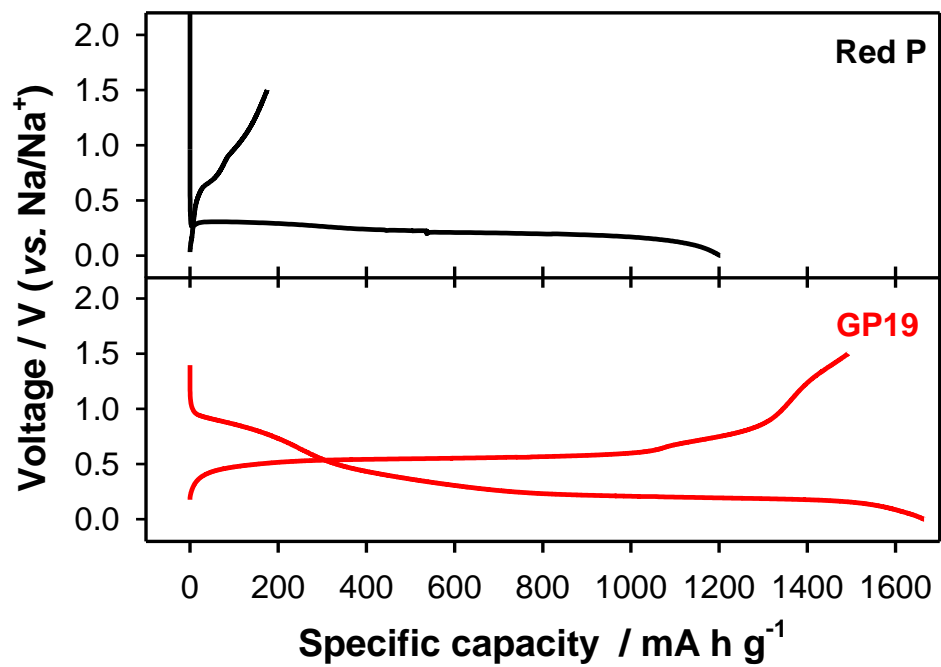
**Figure 7** Voltage profiles of red phosphorus and GP19.

delivered 57% of the theoretical capacity (equivalent to *ca.* 2 mol of Na stored in one mole of P). Also, the initial Coulombic efficiency was 80%. In order to emphasize the carbon effect, the electrochemical performance of the bare amorphous red phosphorus is compared in **Figure 7**. In order to investigate electrochemical reaction mechanism, differential capacity (dQ/dV) and *ex-situ* XRD analysis were performed, respectively. **Figure 8a** shows dQ/dV plots of GP 19 electrode during the $1^{st}$ and $2^{nd}$ cycles. The two reduction peaks are located at about 0.5 and 0.2 V *vs.* Na/Na$^+$, respectively. The 0.5 and 0.2 V *vs.* Na/Na$^+$ reduction peaks are denoted by R1 and R2, respectively. The R1 peak is shown reversible reduction peak during the 1st and 2nd cycles, indicating not electrolyte decomposition but phase transition. To examine phase transition of R1 peak, *ex-situ* XRD was carried out at three points, (i) 0.6, (ii) 0.4 and (iii) 0.35 V *vs.* Na/Na$^+$, as shown in **Figure 8b**. However, new peaks are not observed in *ex-situ* XRD, indicating amorphous phase transition corresponding to R1 peak. The R2 peak is very sharp and delivers most of capacity of GP19. To further clarify phase transition of R2 peak, the cells were disassembled and the *ex-situ* XRD was performed at various points as indicated in the corresponding voltage profile (**Figure 9a**): from 50 % of depth of sodiation to 100 % with increasing 10 % of that (Corresponding to S5 ~ S10). **Figure 9b** shows *ex-situ* XRD of GP 19 electrode at various points with depth of sodiation.
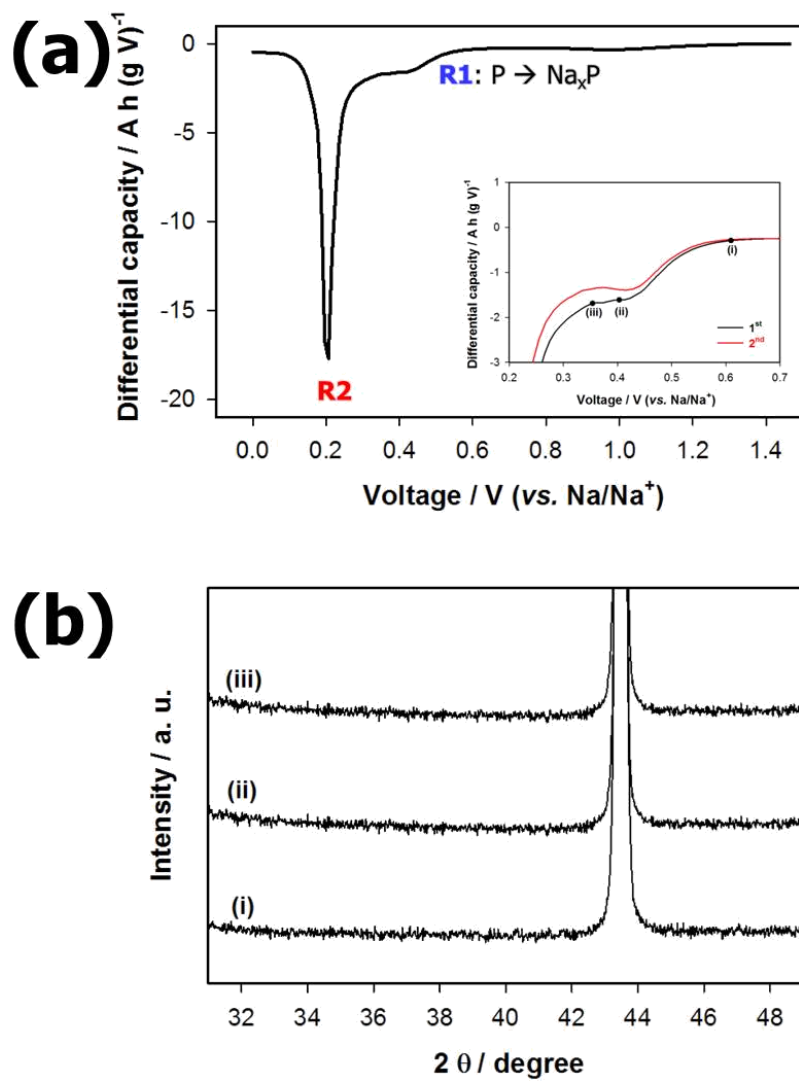
**Figure 8** (a) Differential capacity plot of GP19 during the 1st sodiation (inset: dQ/dV plot of 1st and 2nd sodiation of R1) (b) The *ex-situ* XRD patterns corresponding to inset of (i), (ii) and (iii), respectively.
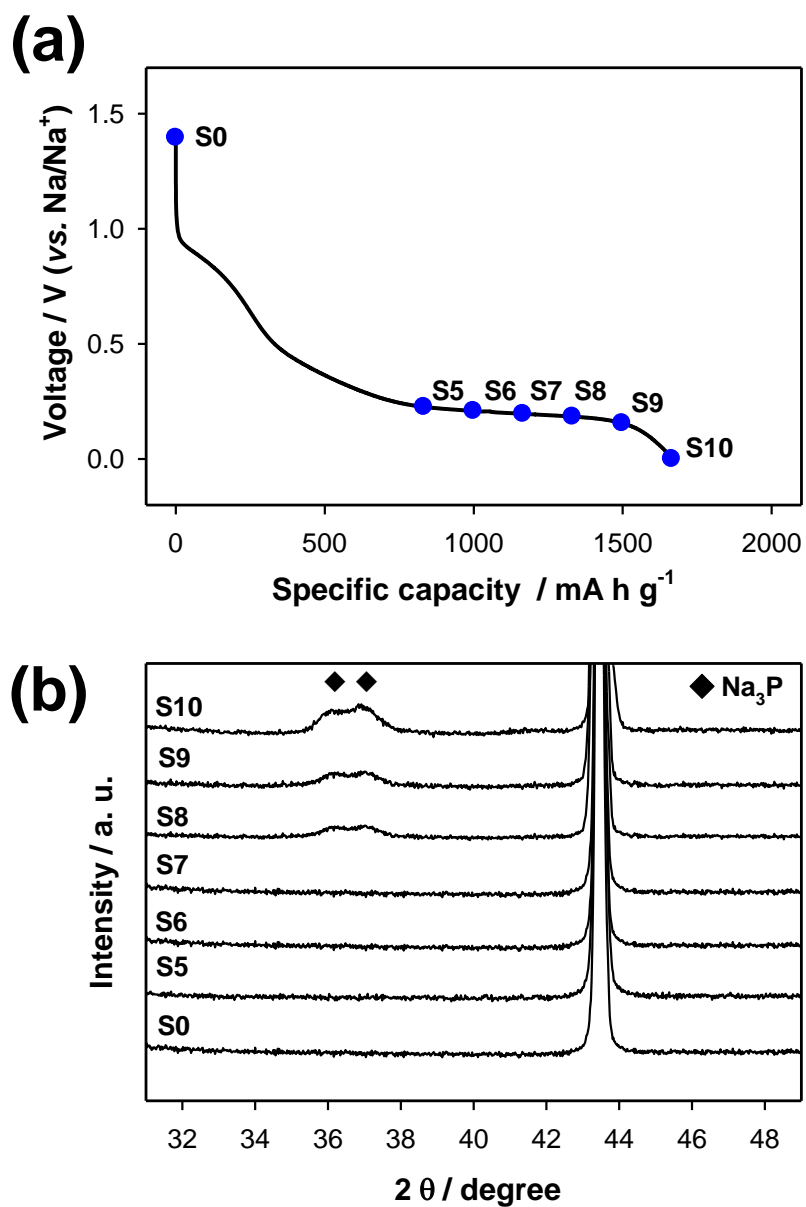
**Figure 9** (a) First sodiation profiles of the GP19 electrode obtained at the different

points indicate depth of sodiation between 50 and 100 %.

(b) Corresponding *ex situ* XRD patterns at each point.

Initially, any other peak was not observed, but the hexagonal crystalline $Na_3P$ (PDF No. 01-073-3917) peak was gradually observed from the S8 (80 % of depth of sodiation). Thus, it is clear that the reduction plateau at *ca.* 0.2 V is ascribed to the formation of $Na_3P$ phase, as shown in *ex-situ* XRD patterns (**Figure 9b**).

 To confirm oxidation reaction with depth of sodiation of GP19 electrode, dQ/dV anaylsis was carried out at various points. Fisrt, Na inserted in phosphorus to potential of S5 ~ S10, respectively, and then Na extracted at 1.5 V *vs*. Na/Na$^+$ (D5 ~ D10). **Figure 10** shows voltage profile of desodiation of GP 19 electrode (D5, D8 and D10) with depth of sodiation (S5, S8 and S10). The voltage profile of D8 is shown slope type, but that of D10 is shown plateau. This result indicates that desodiation voltage profile is different with depth of sodiation. Thus, degree of depth of sodiation could be distinguished based on oxidation process of GP19. In order to investigate clearly, dQ/dV analysis of voltage profile of D5 ~ D10 was performed, as shown in **Figure 11**. Contrary to sodiation, oxidation peak was observed two or three peaks at 0.4 V (O1), 0.55 (O2) V and 0.7 (O3) V *vs*. Na/Na$^+$. It has similar peak from D5 to D7. At the dQ/dV of D8, O2 peak (0.55 V) and three peaks are observed. Further sodiated to D10, O2 peak is more and more distinct. These results are consistent with
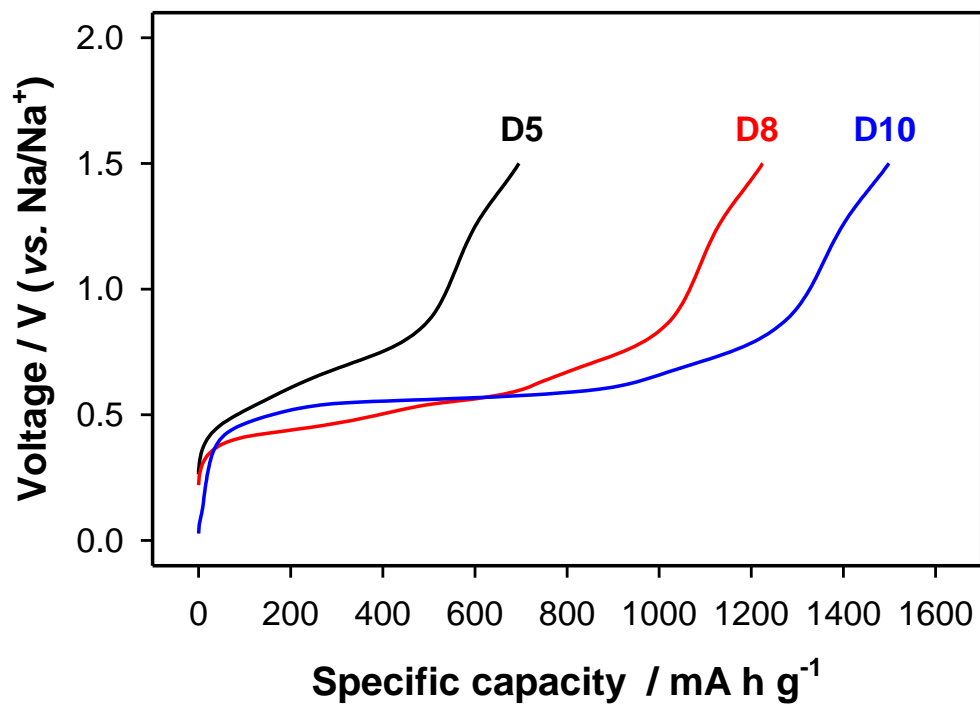
**Figure 10** Desodiation profiles of GP19, which is oxidizing from various depth of

sodiation D5 (50 %), D8 (80 %), and D10 (100 %), respectively.
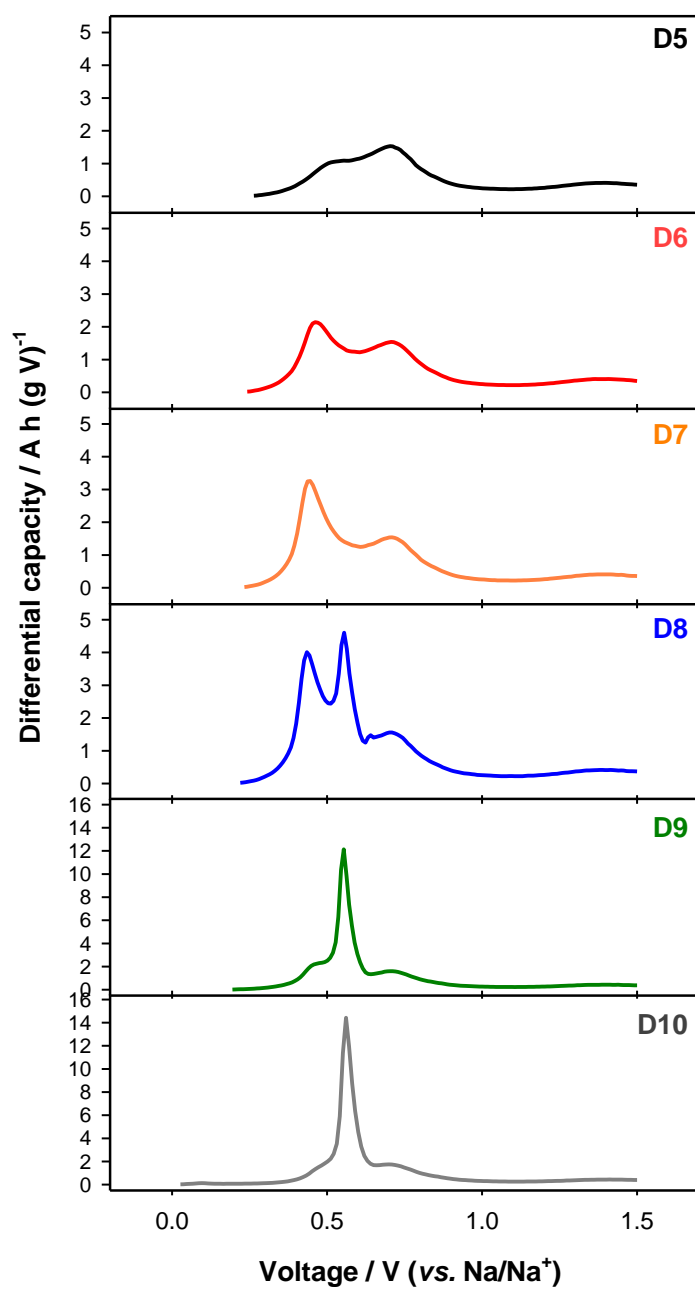
**Figure 11** The dQ/dV analysis of voltage profile from D5 to D10.

*ex-situ* XRD data of sodiation in **Figure 9b**. The dQ/dV plots of D10 shows a sharp peak (O2) during desodiation, indicative of oxidation of $Na_3P$. Also, the crystalline $Na_3P$ is formed in the *ex-situ* XRD from S8 and O2 peak in dQ/dV plots is observed from D8 at the same time. It indicates that the electrochemical reaction of amorphous $Na_xP$ to crystalline $Na_3P$ is biphasic reaction. **Figure 12** presents the voltage curves of a series of GP19 cells that were stopped and disassembled at various states of charge and discharge for *ex-situ* XRD. The *ex-situ* XRD patterns of GP19 electrodes are shown in **Figure 12b**. During the first sodiation plateau, indicative of an amorphous phase appear. At 0 V the new XRD peaks are observed and peaks from a new crystalline $Na_3P$ phase appear. The crystalline phase is gradually amorphization at the desodiation plateau (iv) and fully disappear at full desodiation (v). Thus, amorphous red phosphorus becomes reversible phase transition amorphous to crystalline. The cycle performance of GP19 electrode is displayed in **Figure 13** showing reversible capacity, about 1490 mA h $g^{-1}$ during the initial seven cycles. In addition, the first cycle Coulombic efficiency is *ca.* 80 %. Within the initial seven cycles have relatively stable cycle performance, but drastic capacity fading is observed after the 10th cycles. High capacity alloy based materials are well known to the huge volume changes during charge/discharge result in pulverization and cracking of active materials, leading to rapid capacity fading. In order to
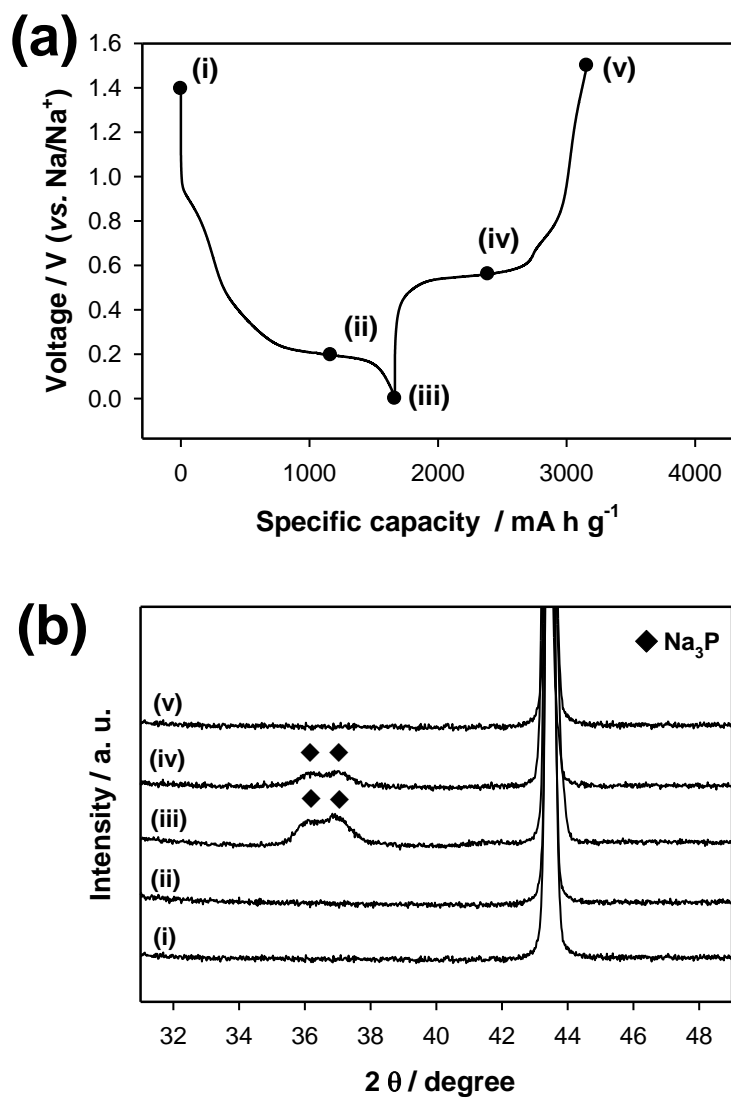
**Figure 12** (a) Voltage profiles of amorphous red P/C composite. (b) The *ex-situ* XRD patterns of GP19 electrodes collected at various points as indicated in (a).
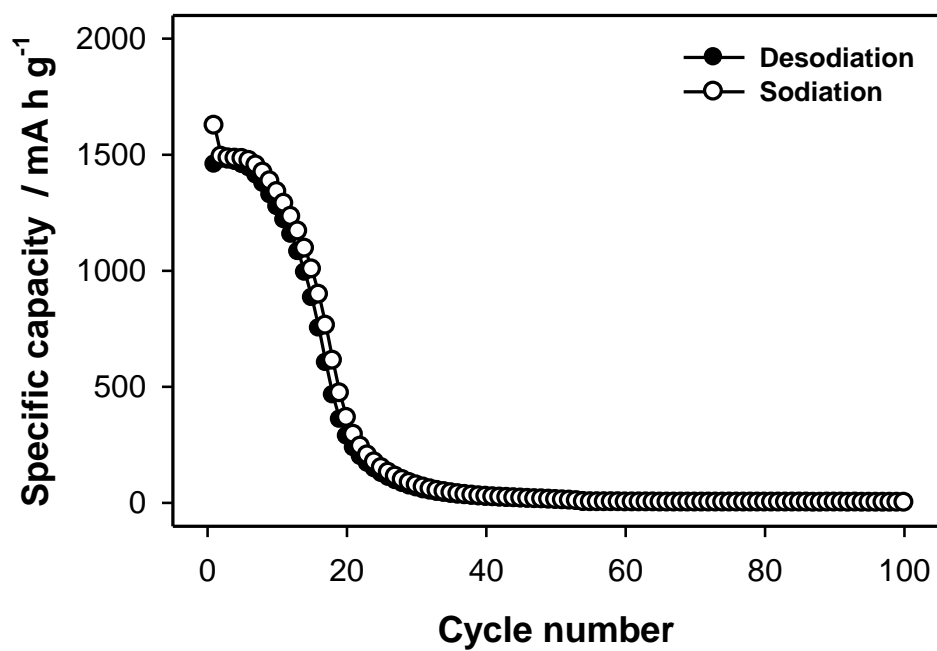
**Figure 13** Cycle performance of GP19 electrode.
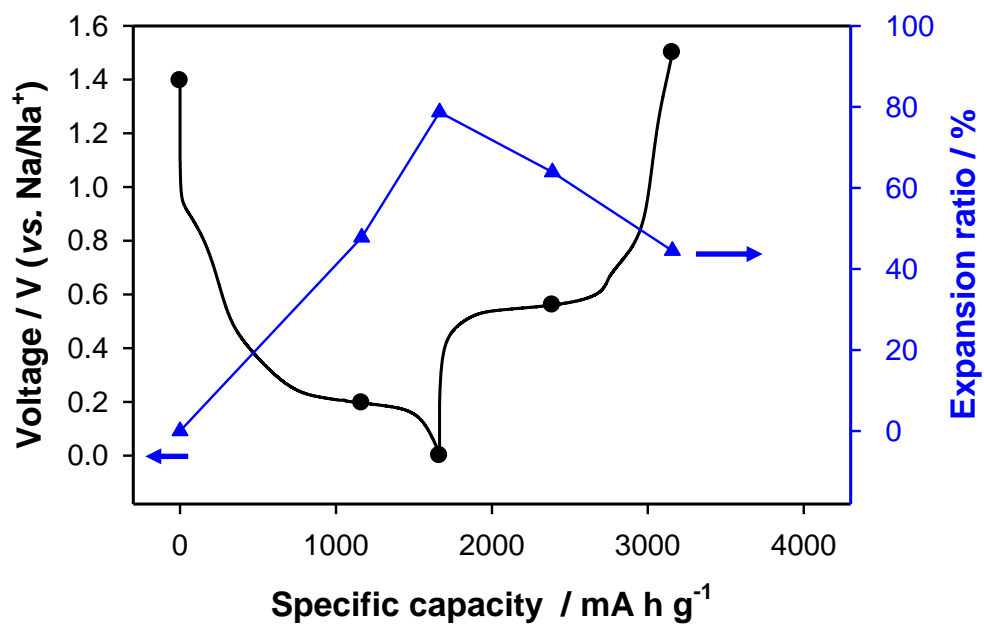
**Figure 14** Voltage profiles (black) of amorphous red P/C composite and the

corresponding electrode thickness change (gray) during sodiation and

desodiation.

confirm the volume change during sodiation and desodiation, the thickness change of electrodes during sodiation and desodiation was measured through *ex-situ* measurement of the electrode thickness (**Figure 14**). The cells were disassembled and the electrode thickness was measured manually at five points (initial, partially-sodiated, fully-sodiated, partially-desodiated, and fully-desodiated state, respectively) in the voltage profile of the GP19 electrode. After full sodiation until the redox potential of the working electrode reached 0 V *vs.* Na/Na$^+$, the thickness of the electrode increased by 80 %. Also, the electrode thickness still remained expanded by 42 % after full desodiation until the redox potential of the working electrode reached 1.5 V *vs.* Na/Na$^+$. The theoretical volume change between P to Na$_3$P is 308 %, which is calculated from the molar volume of red P (14.1 cm$^3$ mol$^{-1}$) and Na$_3$P (57.4 cm$^3$ mol$^{-1}$). This huge volume change is a critical obstacle to improving the electrochemical performance of phosphorus-based materials, as faced in the case of Si-based electrode materials for Li ion batteries.[46-48]

## 4.2. Failure mechanism and improved cycle performance of Phosphorus/carbon composites

Based on the above results, the schematic diagram of the volume change of GP19 particles and electrode with cycling is shown in **Figure 15**. There are two possible points with the failure mechanism of GP19 electrode: (1) loss of electron path; (2) instability of SEI, which resulted from volume changes of GP19 particles during charge and discharge. Initially, the GP19 particles and Super P are well dispersed together in electrode with a large contacting area. In full sodiation, the amorphous red phosphorus undergoes crystallization to $Na_3P$, which involves a significant volume expansion, simultaneously. The volume change of the phosphorus particles will damage the electrode and result in the loss of electrical contact loss between the GP19 and the surrounding matrix. The disconnection of some GP19 particles and the conductive matrix leads to irreversible capacity. Thus, the reversible capacity of the GP19 electrode rapidly decreased with electrochemical reaction. The stability of the SEI on the electrode as large volume change during charge and discharge is another key factor for electrochemical reversibility of sodium-ion batteries. Volumetric changes during the Na insertion/extraction process in phosphorus can easily break the SEI layer. As a result, the additional electrolyte decomposes to cover
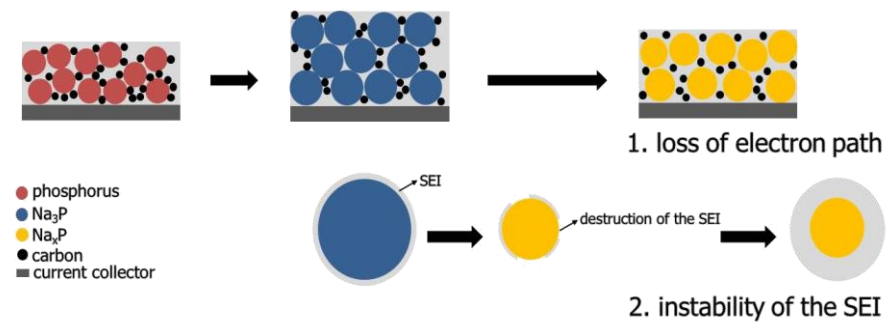
**Figure 15** Schematic diagram of failure mechanism of GP 19 electrode during charge and discharge.

newly exposed surface, leading to increase the thickness of the SEI.

To identify these failure mechanisms in GP19 electrode, desodiation quasi-open-circuit voltage (QOCV) and Coulombic efficiency with cycling were confirmed, as shown **Figure 16**. The thermodynamic voltage of cell can be obtained from rest time for 30 min at the end of desodiation, which is the open-circuit condition due to polarization is zero (current = 0). When the desodiation voltage reached at the cut-off voltage, the current was zero, and the cell was rested to obtain the QOCV. The above-mentioned QOCV experimental was repeated in order to confirm the degree of depth of desoadiation in each cycle. If the decreasing of QOCV is observed, it means the Na trapping in electrode materials due to large polarization by contact loss. **Figure 16** shows decrease of QOCV up to the 50th cycles. It is attributed to Na trapping by contact loss in the electrode continuously. In addition, the Coulombic efficiency steadily decreases, indicating repetitive electrolyte decomposition.

To overcome this failure mode, increasing the graphite ratio in phosphorus/carbon composites and using the fluoroethylene carbonate (FEC) additives, respectively. Increasing the graphite ratio is reduced amount of active phosphorus and retains mechanical strength by carbon matrix, which is related with reduced volume change. Also, FEC additives are well known for stable SEI former as alloy negative electrode materials in Na-ion battery. First, the
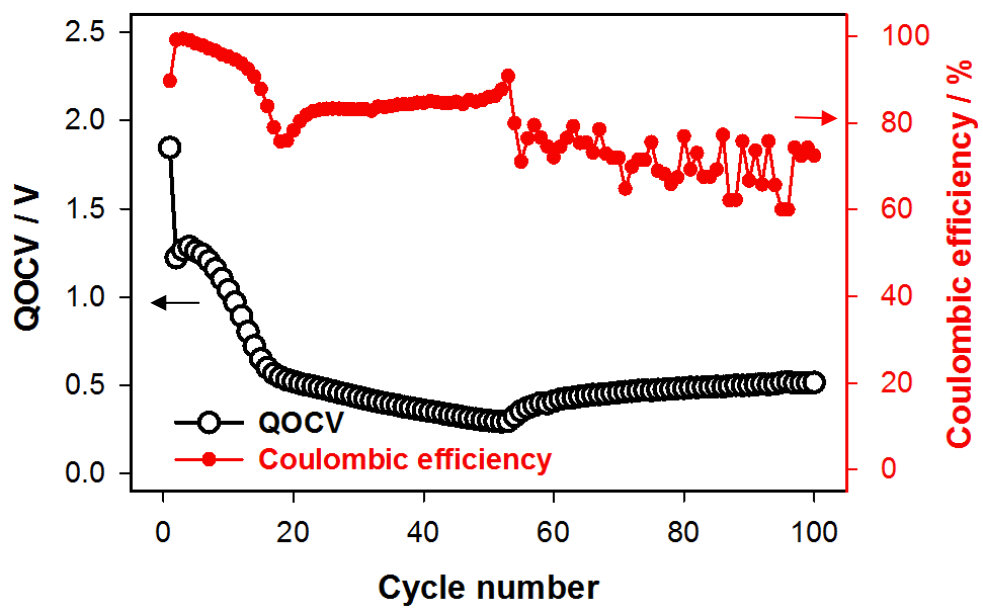
**Figure 16** The quasi-open-circuit voltage and Coulombic efficiency of GP19 electrode

with cycling.

samples of P/C composites prepared GP19, GP37 and GP55, respectively. The electrochemical performance of graphite/phosphorus composites was evaluated using a half cell with a sodium metal without FEC. **Figure 17** shows the cycle performance of the each composite electrode between 1.5 and 0 V at a rate of 200 mA $g_P^{-1}$. The amorphous red phosphorus/graphite composites delivered the 1st desodiation capacity of 1460 (GP19), 1330 (GP37) and 600 (GP55) mA h $g^{-1}$, respectively. With increasing the carbon ratio, cycle performance were much better improved due to reduced volume expansion. (GP19 < GP37 < GP55) To investigate volume change of each electrode, the thickness change of electrodes at full sodiation was measured through *ex-situ* measurement of the electrode thickness (**Figure 18**). After full sodiation until the redox potential of the working electrode reached 0 V *vs.* Na/Na$^+$, the thicknesses of the electrode increased by 79 (GP19), 52(GP37) and 23 % (GP55), respectively. Thus, lower volume expansion of the electrode with increasing the carbon ratio occurs, which leads to enhance cycleability. In addition, the different shape of voltage profiles of each sample is observed (**Figure 19**). Especially, GP55 is not shown plateau at approximately 0.2 V *vs.* Na/Na$^+$. In order to easily identify voltage profile, differential capacity analysis (dQ/dV) was carried out shown in **Figure 20a**. The three samples are shown reduction peak near 0.2 V *vs.* Na/Na$^+$ in sodiation. However, R2 peak of GP37 and GP55 are broader and lower
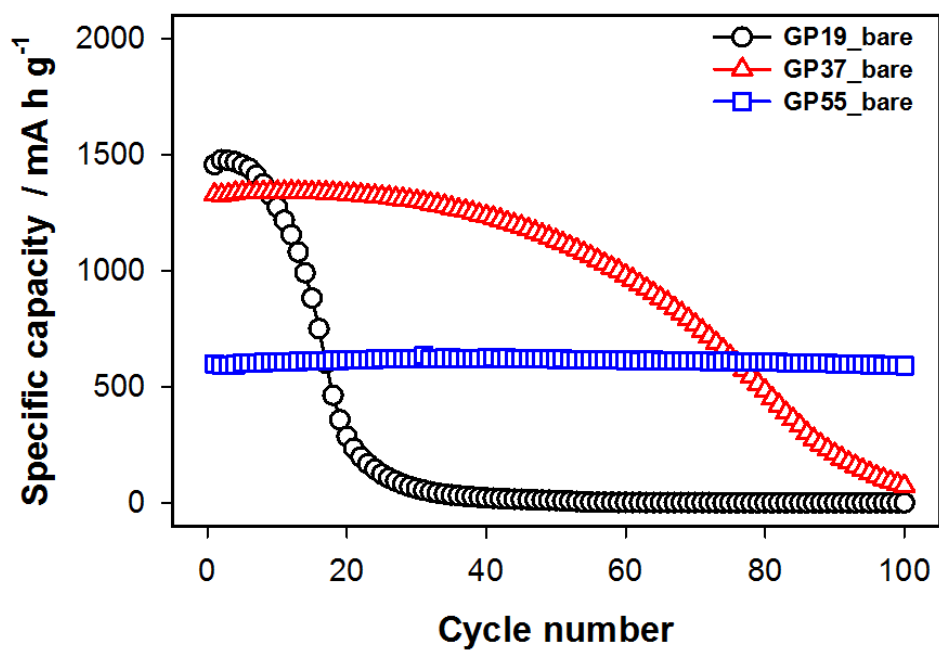
**Figure 17** Cycle performance of GP19, GP37, and GP55 electrode, respectively.
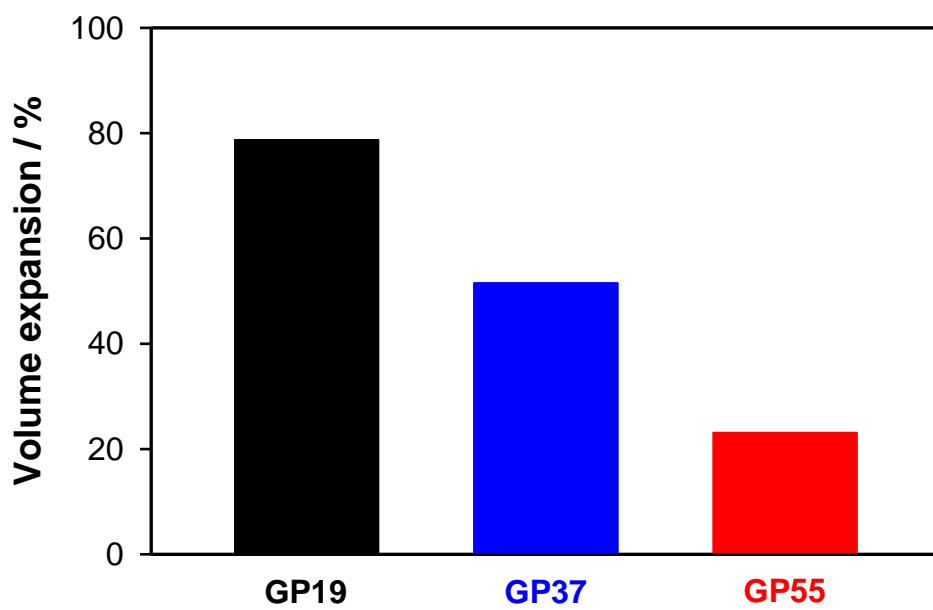
**Figure 18** Volume expansion of GP19, GP37, and GP55 electrodes during sodiation, respectively.
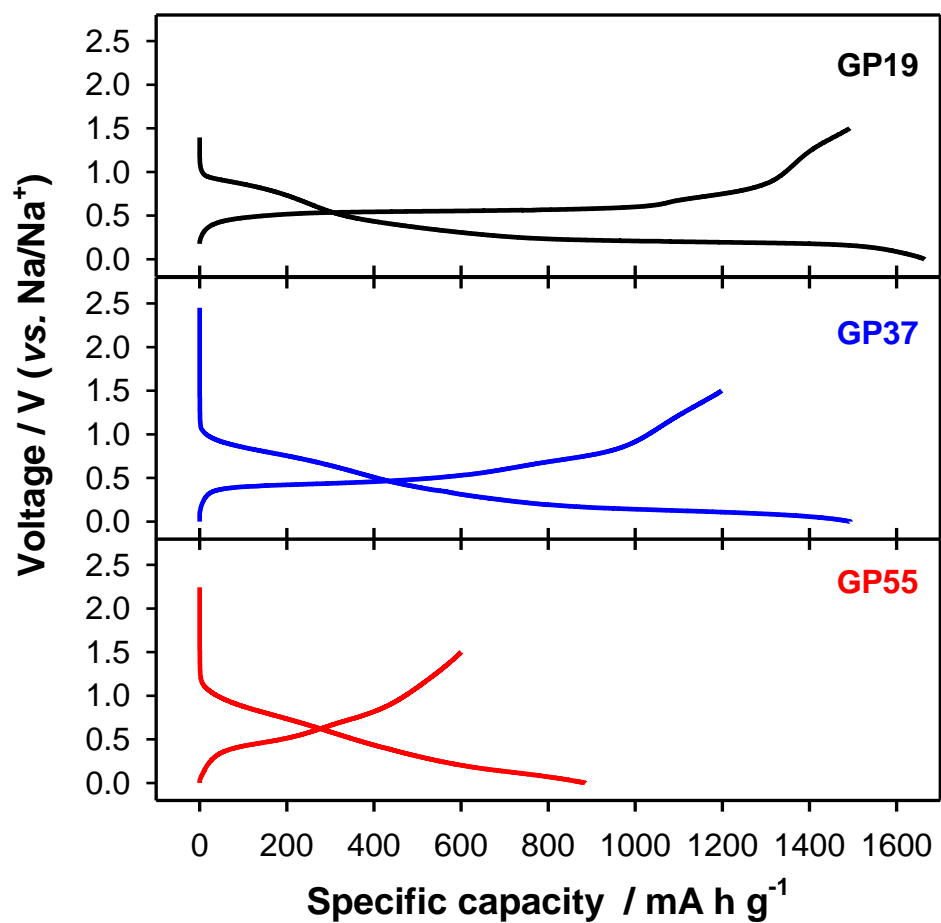
**Figure 19** Voltage profile of GP19, GP37, and GP55 electrodes, respectively.
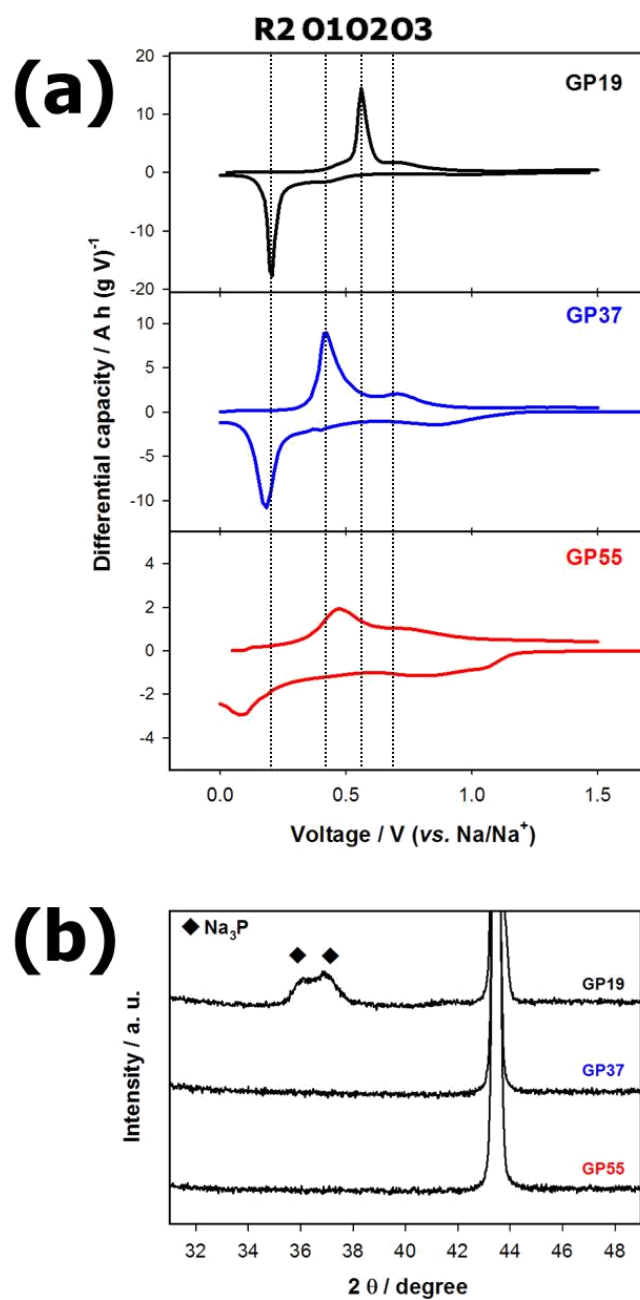
**Figure 20** (a) Differential capacity plots (dQ/dV) and (b) sodiation *ex-situ* XRD patterns of GP19, GP37, and GP55 electrode, respectively.

potential shift than that of GP19 during reduction process. This result indicates that increasing graphite content impede the insertion of Na ions into the phosphorus, which leads to decrease depth of sodiation. The decreasing depth of sodiation with increasing carbon contents is consistent with dQ/dV plots of oxidation peak and *ex-situ* XRD at the full sodiation shown in **Figure 20a** and **20b**, respectively. In dQ/dV plots in desodiation (**Figure 20a**), oxidation peak at 0.55 V corresponding to $Na_3P$ is only observed in GP19 electrode. Also, **Figure 20b** presents phase transition of $Na_3P$ at the full sodiation in *ex-situ* XRD, which is shown in GP19 electrode, not GP37 and GP55. That is, decreasing depth of sodiation as well as reducing phosphorus amount and increasing carbon buffer matrix alleviated volume expansion of GP electrode. Consequently, optimization of carbon to phosphorus ratio is extremely important in order to enhance electrochemical performance and GP37 is more possible than GP55 for using high capacity negative electrode materials. In case of the GP55 electrode is low density due to high carbon contents and low specific capacity due to high resistance by high carbon ratio, it is not appropriate to use high negative electrode materials for sodium-ion battery in spite of highly reversible cycle performance. However, the long-term cycle performance of GP37 must be complementary. In order to improve long-term cycleability, examine and compare Na cell performance with organic electrolyte

additives. The organic additives such as fluoroethylene carbonate (FEC) are well known to form SEI layers in silicon negative electrode materials as high volume expansion during lithiation for lithium-ion battery.[49-51] In addtition, the electrolytes containing FEC is more superior to cycling stability in sodium-ion battery.[20,45,52-54] In this study, to optimize the cell performance, FEC additives added in EC:DEC electrolytes. **Figure 21** compared with the cycle performance and Coulombic efficiency of pristine and containing FEC. Both cell delivered the similar reversible capacity of about 1300 and 1200 mA h g$^{-1}$, respectively, when an fluoroethylene carbonate (FEC) additive was used, but FEC added electrolyte showed much more improved cycle performance than pristine, as shown in **Figure 21a**. Moreover, FEC added cell exhibited negligible capacity fading over 100 cycles and high Coulombic efficiency over 99 % in **Figure 21b**. Without the FEC additive, GP37 delivered a higher reversible capacity of about 1300 mA h g$^{-1}$, but showed worse cycle performance. As is well known, this indicates that the FEC additive forms stable SEI layers, resulting in excellent cycle performance of GP37 electrode. To identify the decomposition products formed on the GP37 electrode, *ex- situ* X-ray photoelectron spectroscopy (XPS) measurements of the electrode were carried out at the first cycle (**Figure 22a**). The electrodes cycled with FEC additive, the NaF is observed in the F1s spectra at energy about 685 eV. The improved cycle performance was also suggested
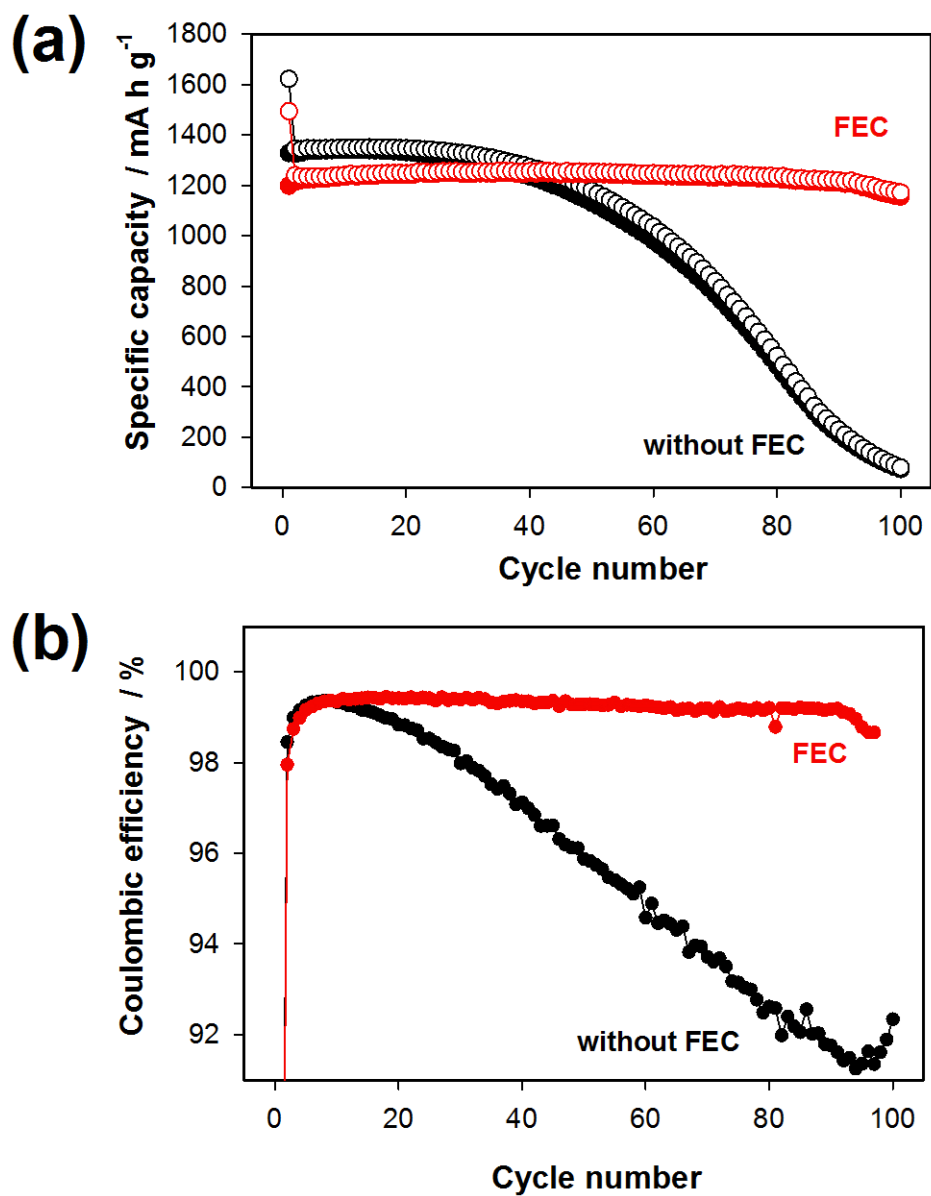
**Figure 21** (a) Cycle performance and (b) Coulombic efficiency of GP 19 with or without FEC, respectively.
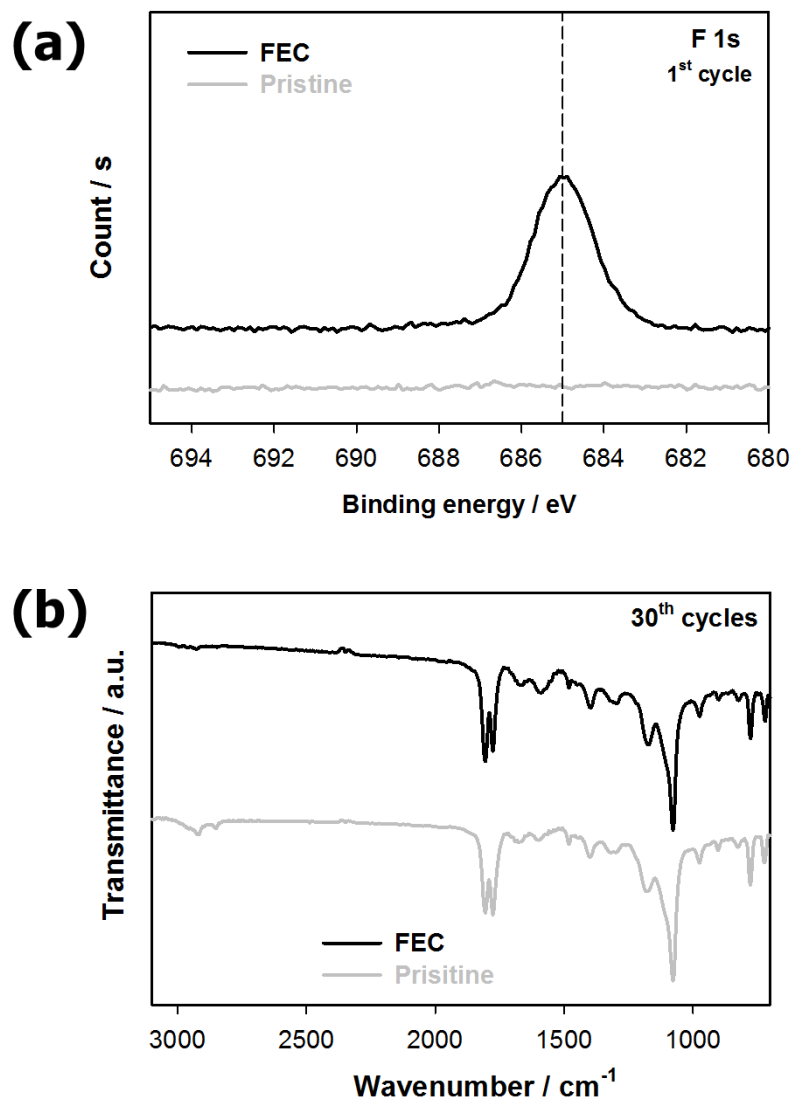
**Figure 22** The surface analysis of GP 37 electrode with or without FEC, respectively.

(a) *ex-situ* XPS at the 1$^{st}$ cycle and (b) FT-IR at the 30$^{th}$ cycles.
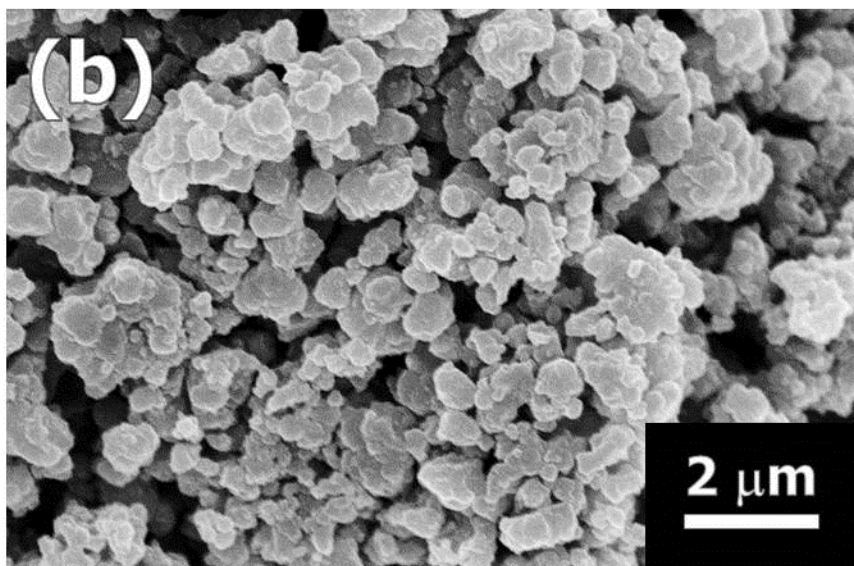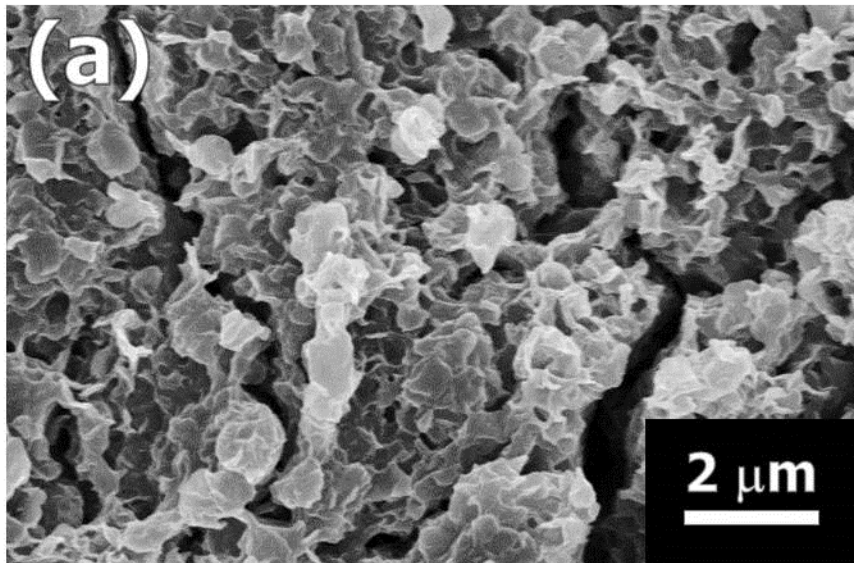
**Figure 23** FE-SEM images of GP37 electrode (a) without FEC and (b) with FEC at the 50th cycles, respectively.

to be caused by the formation of stable and thin NaF-like SEI layers due to the addition of the FEC additive.[20,53,54] However, NaF-like SEI layers obtained from the FEC additive increases a resistance,[45,55] owing to an increase of polarization and these results in a lower reversible specific capacity, which elucidate later. Also, in order to further investigate SEI for long-term cycle, Fourier transform infrared (FT-IR) spectroscopy analysis was performed at the 30th cycles. **Figure 22b** shows comparison of *ex-situ* FT-IR spectra of pristine and FEC added GP37. Clear differences in the SEI products formed in each electrolyte were identified from FT-IR spectra. The measured spectra from electrodes after 30 cycled in EC-DEC electrolyte contain the expected peaks of $(CH_2OCO_2Na)_2$, which is a major reduction product of EC.[50,55-57] The spectra of FEC added solvent are similar to that of EC-DEC. However, a major difference between the spectra related to two solvents is around 3000 cm^{-1} peak corresponding to EC decomposition.[50,57] This result is consistent with the observation of the *ex-situ* FE-SEM at the 50th cycle showing the formation of the SEI layer (**Figure 23**). The surface of GP37 electrode using EC-DEC electrolyte shows denser than using that of FEC added electrolyte. Thus, FEC added electrolyte minimizes EC decomposition at the electrode surfaces. As previously described, NaF-like SEI derived FEC is known to resistive film. This is consistent with the electrochemical characteristics with and without FEC,

respectively. **Figure 24a** shows the charge-discharge voltage profiles of the GP19 electrodes with and without FEC between 1.5 and 0 V *vs.* Na/Na$^+$ at a rate of 200 mA g$_P^{-1}$, respectively. The GP37 electrode delivered reversible capacity at the first cycle of 1200 and 1327 mA h g$^{-1}$ in FEC containing and EC-DEC electrolyte, respectively. The lower specific capacity is observed in FEC containing electrolyte. Also, dQ/dV plots of GP37 electrode in FEC containing electrolyte shows lower reduction potential approximate 70 mV than that of FEC free in shown in **Figure 24b**.

To further confirm the effect of resistive NaF-like layer to electrochemical characteristics for long-term cycling, comparison of differential capacity analysis (dQ/dV) with cycling of FEC added and pristine electrolyte are performed, as shown in **Figure 25** and **Figure 26**, respectively. Initially, two oxidation peaks are observed both with and without FEC. Interestingly, additional peak (O2) corresponding to Na$_3$P is gradually observed with cycling. The formation of Na$_3$P is related that the particle is cracked and pulverized by the repeated volume change of GP37 with cycling, resulting in shorten diffusion path due to reduced particle size. Due to these features, the polarization of electrode decreases with cycling and the phosphorus can be sodiated up to Na$_3$P. The increasing capacity for 10 cycles should be elucidated by the crack and pulverization mechanism. Furthermore, the similar dQ/dV peak shape is
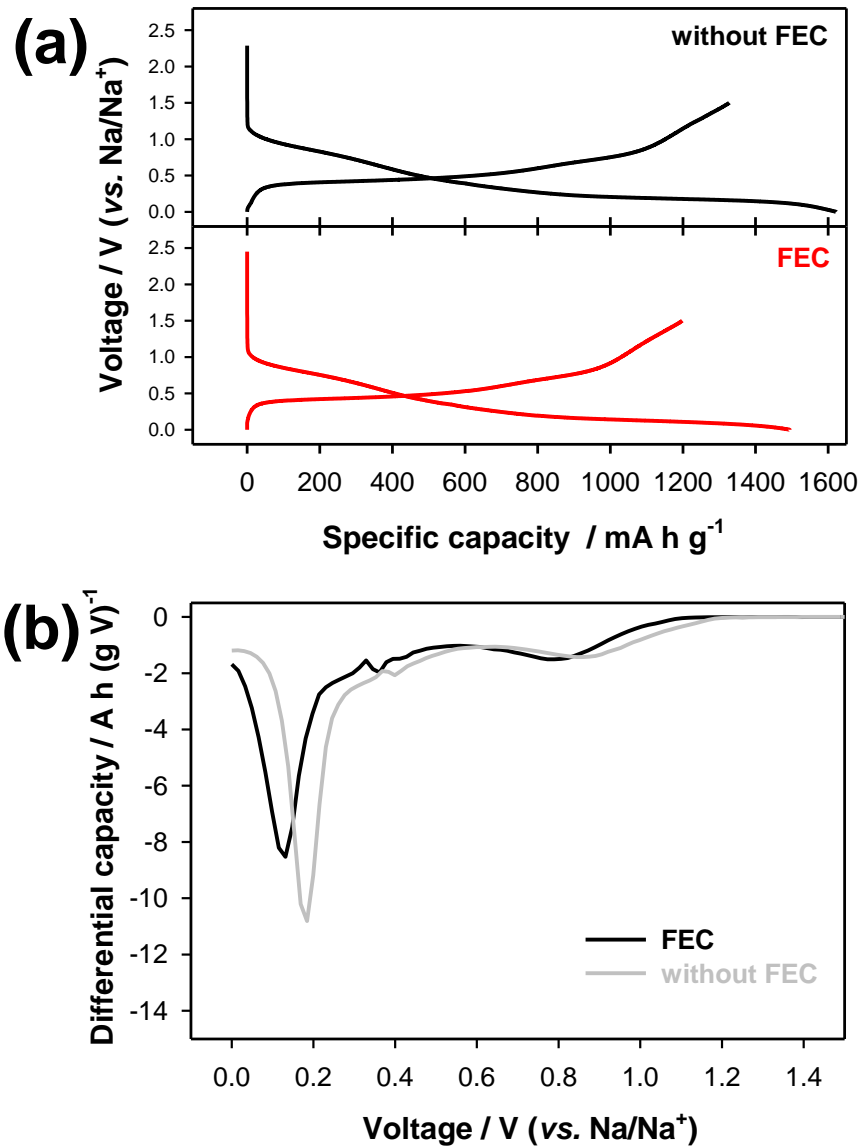
**Figure 24** (a) Voltage profile and (b) sodiation dQ/dV plot of GP37 electrode with or
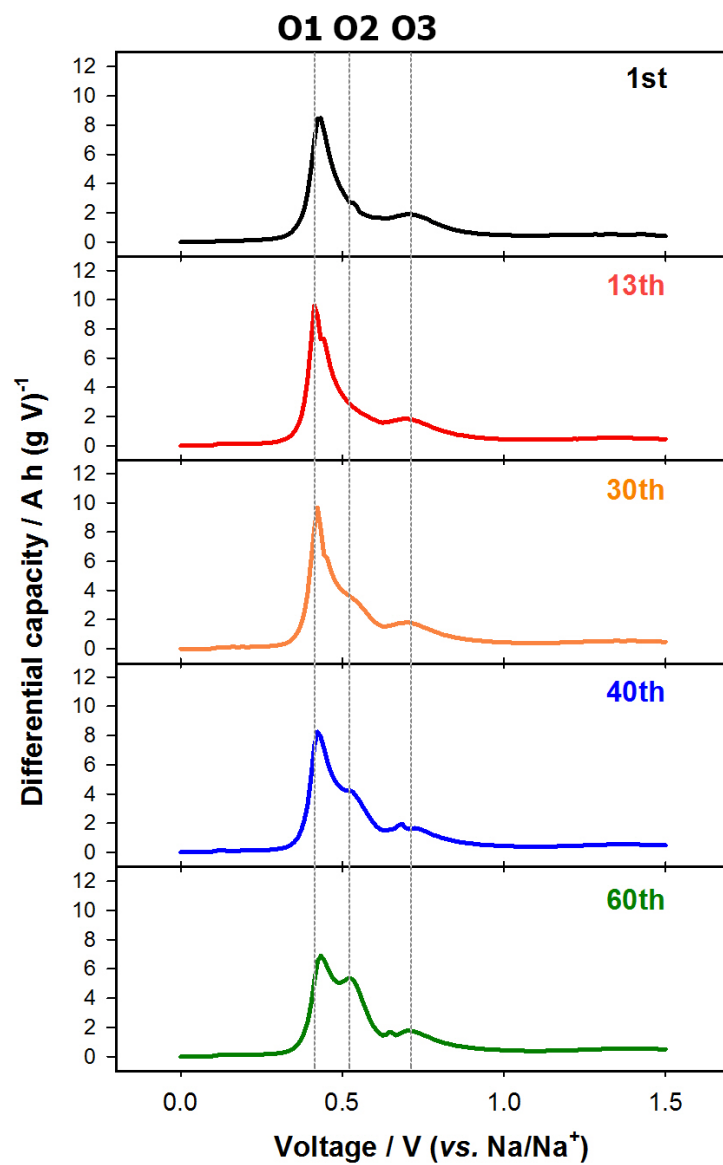
without FEC

**Figure 25** Differential capacity plots of GP37 electrode with FEC at the various cycles during desodiation
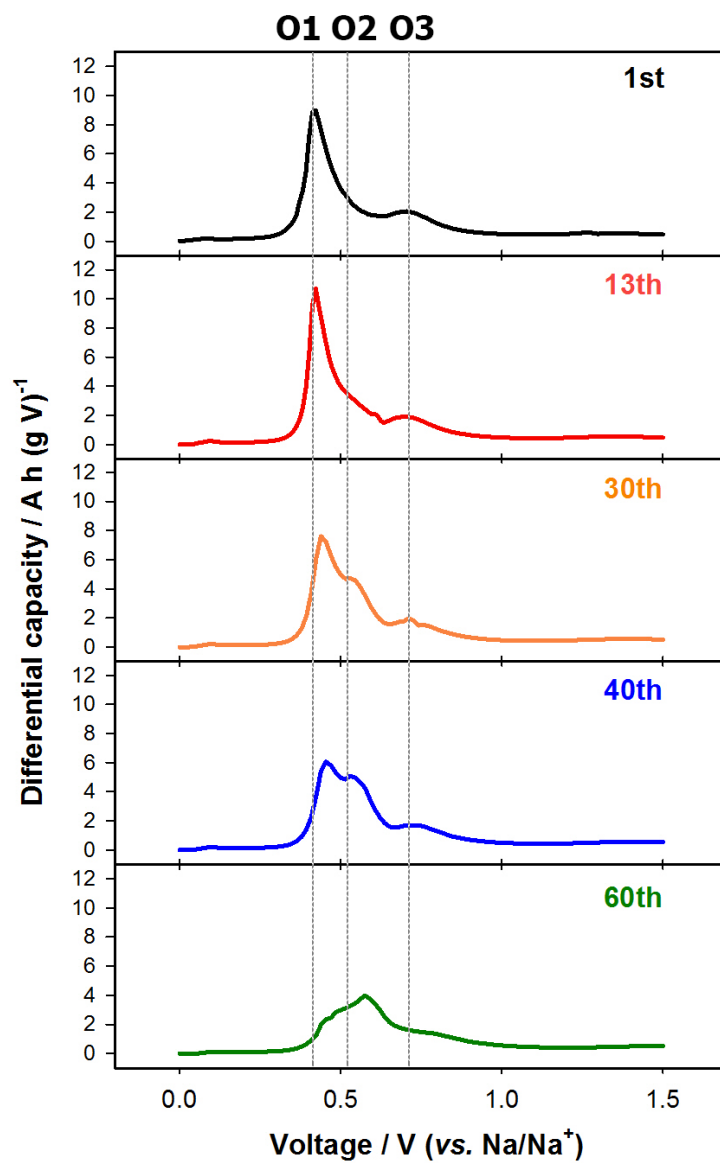
**Figure 26** Differential capacity plots of GP37 electrode without FEC at the various

cycles during desodiation

observed at the $40^{th}$ (FEC) and $30^{th}$ (pristine) cycle, respectively. They show three oxidation peaks including $Na_3P$ peaks. It means (1) difference of depth of sodiation and (2) occurrence of inhomogeneous sodiation at the electrode in the two electrolyte, which is formation both $Na_xP$ and $Na_3P$ phase, respectively. The formation of $Na_3P$ at the further cycles in the FEC containing electrolyte comparing to without FEC is related with depth of sodiation. The GP37 electrode in FEC-containing electrolyte is lower depth of sodiated in phosphorus than that of pristine due to increase of polarization by NaF-like SEI layers obtained from FEC additives. It leads to lower volume change and cracking during charge and discharge, resulting in formation of $Na_3P$ at the further cycles than pristine electrolyte. However, there is a stark difference between the two after the formation of $Na_3P$ peak. The electrode of FEC added electrolyte retains its cycle performance for 100 cycles, but that of pristine electrolyte shows capacity fading. Thus, SEI derived FEC is more stable than that of pristine. In addition, though the area of $Na_3P$ peak has been increasing since the $40^{th}$ cycle, capacity retains for the 100 cycles. Because more sodiated to $Na_3P$ in partial particle which is reduced size by cracking and pulverization, GP37 electrode in FEC containing electrolyte comes across as it shows good capacity retention but it does really not.

Interestingly, there is no increasing the specific capacity with FEC despite further sodiated to $Na_3P$. Assuming using SOC completely in this system is 100 %, and this shows it is only possible to use 60 % of SOC in GP37. At the first cycle of sodiation, Na is inserted about 60 %. And then the nth cycle such as the 40th cycle, it delivered similar capacity with the previous cycles. Because it is not observed capacity fading, Na is inserted to amorphous $Na_xP$ the same capacity and a little portion of electrode material is further sodiated to $Na_3P$. However, there is no increasing capacity. It indicates that the increasing capacity by formation of $Na_3P$ is concurrent with degradation with cycling. Thus, it makes up for its capacity and looks like good cycle performance of electrode materials.

The failure mechanism of GP37 with and without FEC is summarized in a schematic diagram (**Figure 27**). After long-term cycling, there are thick SEI derived EC decomposition in pristine EC:DEC electrolyte and NaF-like SEI film derived FEC reduction in FEC added electrolyte. These passivating films by EC decomposition lead to cell degradation and the NaF-like SEI film is stable SEI. Also, it shows inhomogeneous sodiation by pulverization and cracking and observation of different depth of sodiation by surface film resistance.
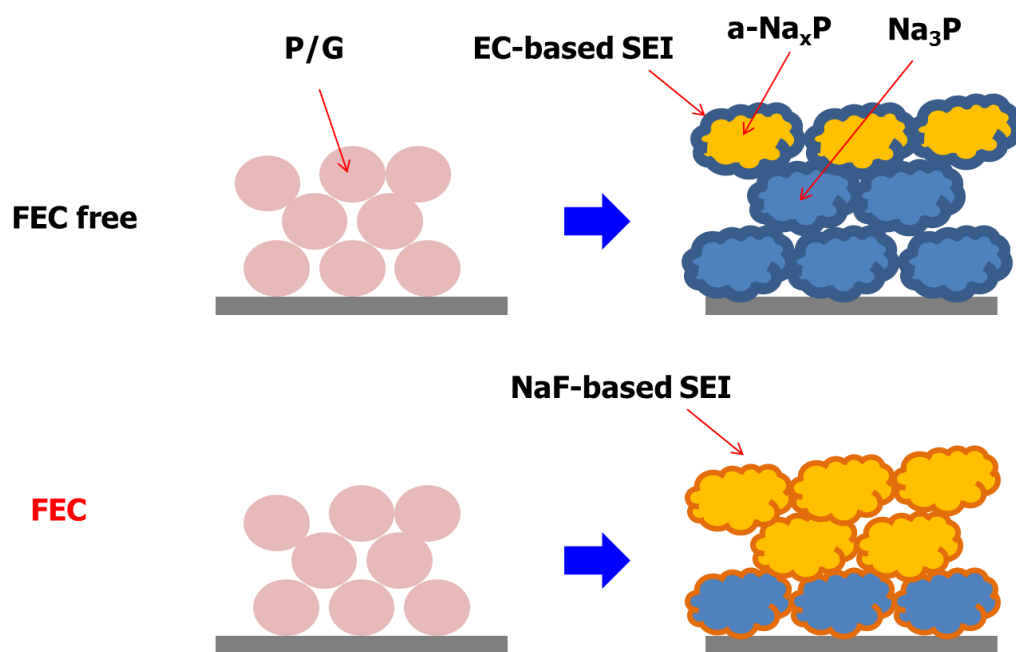
**Figure 27** Schematic diagram of comparison of reaction mechanism with cycling of FEC added and pristine electrolyte.

## 4.3. Tin phosphide as High volumetric capacity negative electrode for Sodium-ion battery

Na-ion batteries have recently attracted a great deal of attention as a next-generation battery, because Na resources are inexhaustible and cheaper than Li resources. However, although Na-ion batteries have shown promising electrochemical performance including stable cycleability and good rate capability, it should be stressed that it is not easy for Na-ion batteries to replace Li-ion batteries owing to the critical issue of Na-ion batteries having slightly lower energy density than Li-ion batteries.[58-62] The lower energy density of Na-ion batteries is attributed to the lower specific capacity and redox potential of most Na-ion insertion materials that have been introduced to date. Therefore, in order to successfully replace Li-ion batteries by Na-ion batteries, new negative electrode (anode) materials having a high specific capacity and low redox potential should be introduced. Recently, there have been a few studies on Na-ion insertion materials for use in anodes with a high specific capacity. For examples, Sn-[30,31,63-67] and Sb-[32,44,68-72]based materials have been examined as promising anode materials, and they delivered a high reversible capacity of approximately 500 ~ 700 mA h g$^{-1}$. While Sb-based materials exhibited stable cycle performance, Sn-based materials showed poor
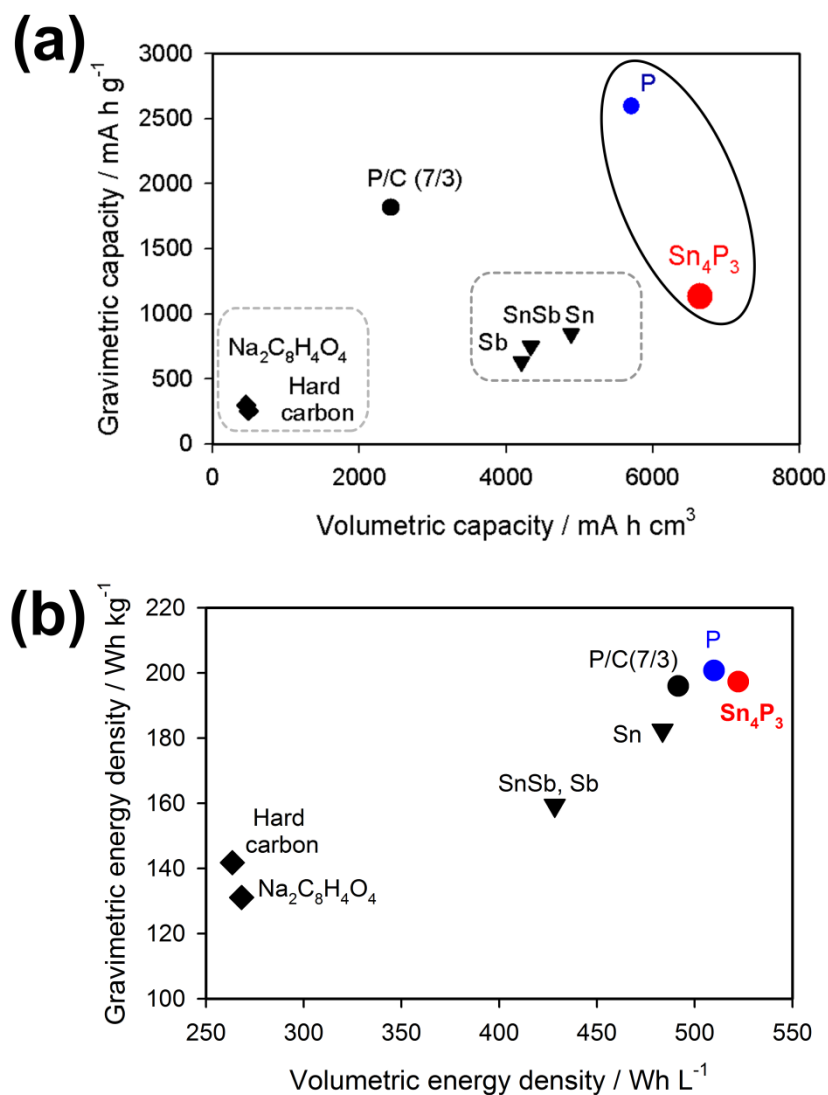
**Figure 28** Theoretical (a) volumetric and gravimetric specific capacities and of various negative electrode materials for Na-ion batteries and (b) volumetric and gravimetric energy densities for full cells with various negative electrode materials.

reversibility. However, the redox potential of Sn is lower than that of Sb, and thus, Sn-based materials are more beneficial for obtaining higher energy density (working voltage). Also, phosphorus/carbon composite materials have shown excellent electrochemical performance including the highest specific capacity (1890 mA h $g^{-1}$) among all reported anode materials.[73-78] However, phosphorus has poor electrical conductivity, and thus, a large amount of carbon (～30 wt.%) has to be used in the phosphorus/carbon composites to enhance their electrical conductivity, which decreases their gravimetric and volumetric energy densities. The volumetric energy density of a battery is one of the most critical factors that determine its suitability as a next generation battery for use in electric vehicles and mobile devices. Therefore, it is important to develop new electrode materials delivering high volumetric specific capacity for Na-ion batteries. In this study, $Sn_4P_3$ was examined for the first time as an anode material for Na-ion batteries. The theoretical volumetric capacity of $Sn_4P_3$ is 6650 mA h $cm^{-3}$, which is much higher than that of a phosphorus/carbon (7:3 wt. ratio) composite (2431 mA h $cm^{-3}$) and even higher than that for bare phosphorus (5710 mA h $cm^{-3}$), as shown in **Figure 28a**. This volumetric capacity of $Sn_4P_3$ is the highest among Na-ion insertion materials reported to date. **Figure 28b** also represents the gravimetric and volumetric energy densities for full cells composed of various anode materials and the cathode material of P2-

Na$_{2/3}$[Fe$_{1/2}$Mn$_{1/2}$]O$_2$.[79] Moreover, the electrical conductivity of Sn$_4$P$_3$ is 30.7 S cm$^{-1}$, which is much higher than that of a phosphorus/carbon (7:3 wt. ratio) composite (3.5 × 10$^{-5}$ S cm$^{-1}$).[73] Accordingly, carbon-containing composites can be dispensed with Sn$_4$P$_3$. It was previously thought that Sn$_4$P$_3$ was not a promising anode material for Li-ion batteries because of its poor cycle performance and relatively high redox potential as an anode. Thus, only a few studies have focused on the just lithiation and delithiation reaction mechanism of Sn$_4$P$_3$,[80,81] although various metal phosphide materials have been extensively studied for use in Li-ion batteries.[82-91] However, in this study, Sn$_4$P$_3$ as an anode for Na-ion batteries shows excellent electrochemical performance. Sn$_4$P$_3$ delivered a high reversible capacity of 718 mA h g$^{-1}$, and showed very stable cycle performance with negligible capacity fading over 100 cycles; the cycle performance of Sn$_4$P$_3$ was better than those of previously reported Sn-based materials and phosphorus/carbon composites. Moreover, Sn$_4$P$_3$ delivered its reversible capacity at an appropriately low redox potential of about 0.3 V *vs.* Na/Na$^+$. The redox potential of Sn$_4$P$_3$ is lower than that of phosphorus, indicating that the energy density of a full cell with a Sn$_4$P$_3$ anode would be higher than that of a full cell with a phosphorus anode when assumed that both anode materials deliver equal reversible capacities. An intermetallic
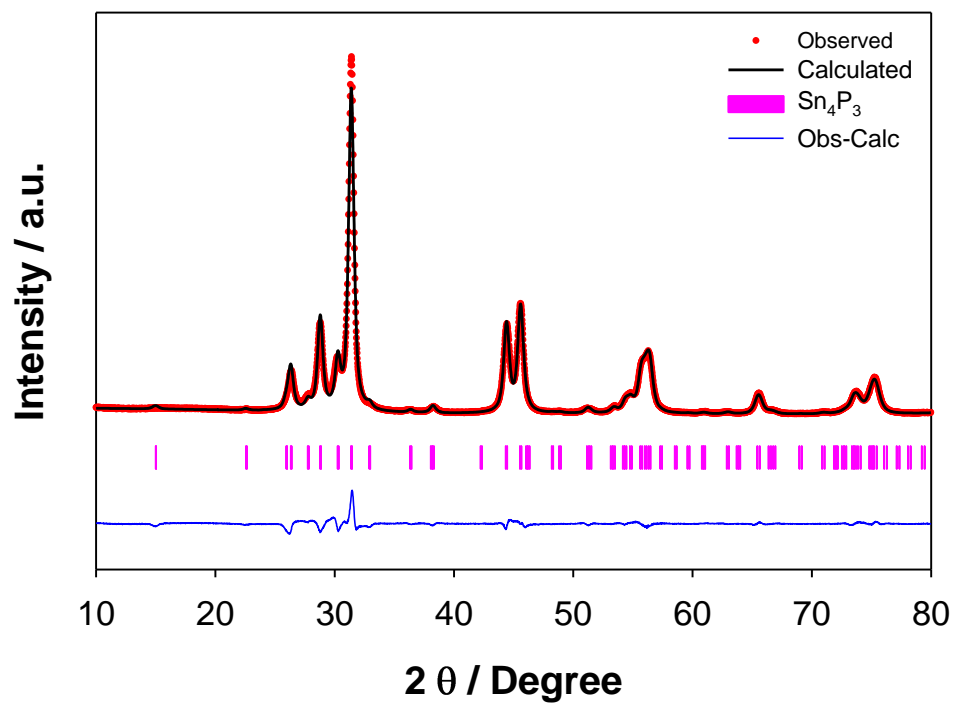
**Figure 29** X-ray diffraction pattern and the corresponding Rietveld refinement of $Sn_4P_3$.

**Table 1** The lattice parameters of $Sn_4P_3$ compounds obtained from Rietveld refinement.

| | a [Å] <br> b [Å] <br> c [Å] | α <br> β <br> γ | Volume[Å$^3$] | $R_p$ [%] | $R_{wp}$ [%] | $R_F^2$[%] | $\chi^2$ |
|---|---|---|---|---|---|---|---|
| **$Sn_4P_3$** | 3.98213(20) <br> 3.98213 <br> 35.4490(23) | 90.0 <br> 90.0 <br> 120.0 | 486.82(6) | 5.21 | 6.90 | 1.96 | 18.40 |
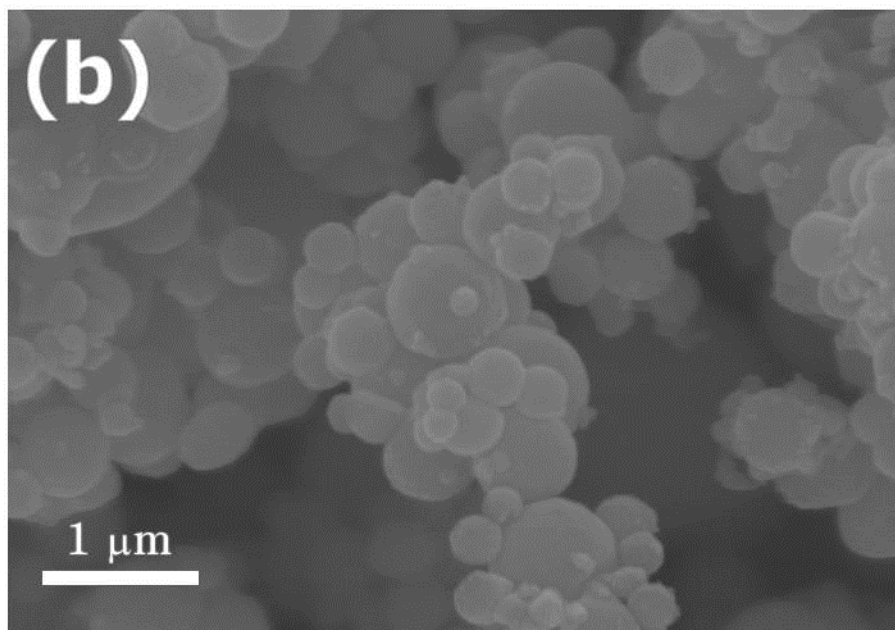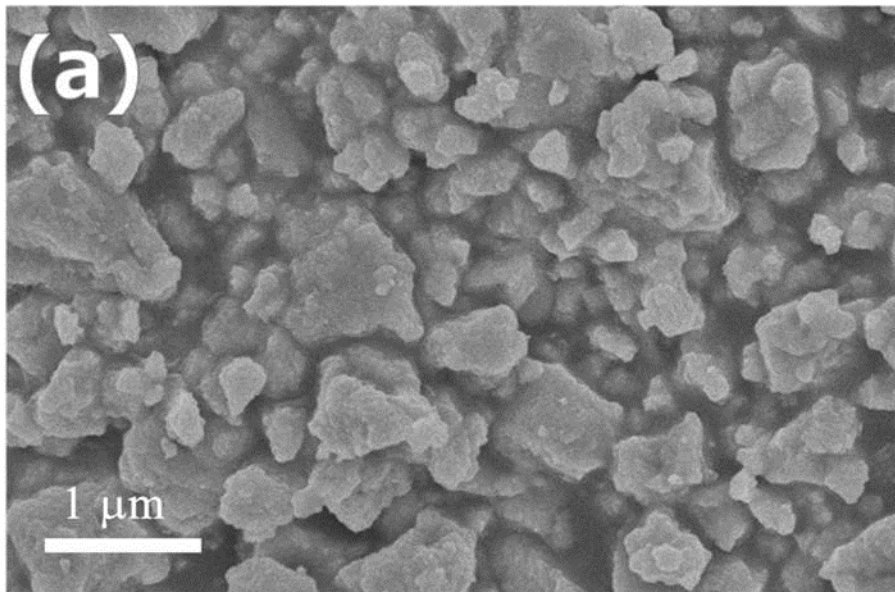
**Figure 30** FE-SEM images of (a) tin phosphide and (b) tin.

compound of $Sn_4P_3$ was obtained by facile high-energy mechanical ball milling in an Ar atmosphere for an hour. **Figure 29** shows the X-ray diffraction (XRD) pattern and the corresponding Rietveld refinement of as-prepared $Sn_4P_3$ powders, and no impurity was observed. The lattice parameter and agreement factors of $Sn_4P_3$ powders obtained from Rietveld refinement is given in **Table 1**. The space group of the $Sn_4P_3$ crystal structure is *R-3m*, and $Sn_4P_3$ crystallizes in a rhombohedral lattice.[92] The electrochemical performance of the $Sn_4P_3$ electrode was evaluated using a half cell with a sodium counter electrode. **Figure 31** shows a comparison of the cycle performance and voltage profiles of Sn and $Sn_4P_3$. Both electrodes delivered a similar reversible capacity of about 718 mA h $g^{-1}$ when an fluoroethylene carbonate (FEC) additive was used, but $Sn_4P_3$ showed much more improved cycle performance than Sn, as shown in **Figure 31**. Moreover, $Sn_4P_3$ exhibited negligible capacity fading over 100 cycles in spite of its larger micrometer-sized particles (**Figure 30a**) than nanosized Sn particles (**Figure 30b**). Without the FEC additive, $Sn_4P_3$ delivered a higher reversible capacity of about 833 mA h $g^{-1}$, but showed worse cycle performance. As is well known, this indicates that the FEC additive forms stable SEI layers, resulting in excellent cycle performance of $Sn_4P_3$. However, NaF-like SEI layers obtained from the FEC additive increases a charge-transfer
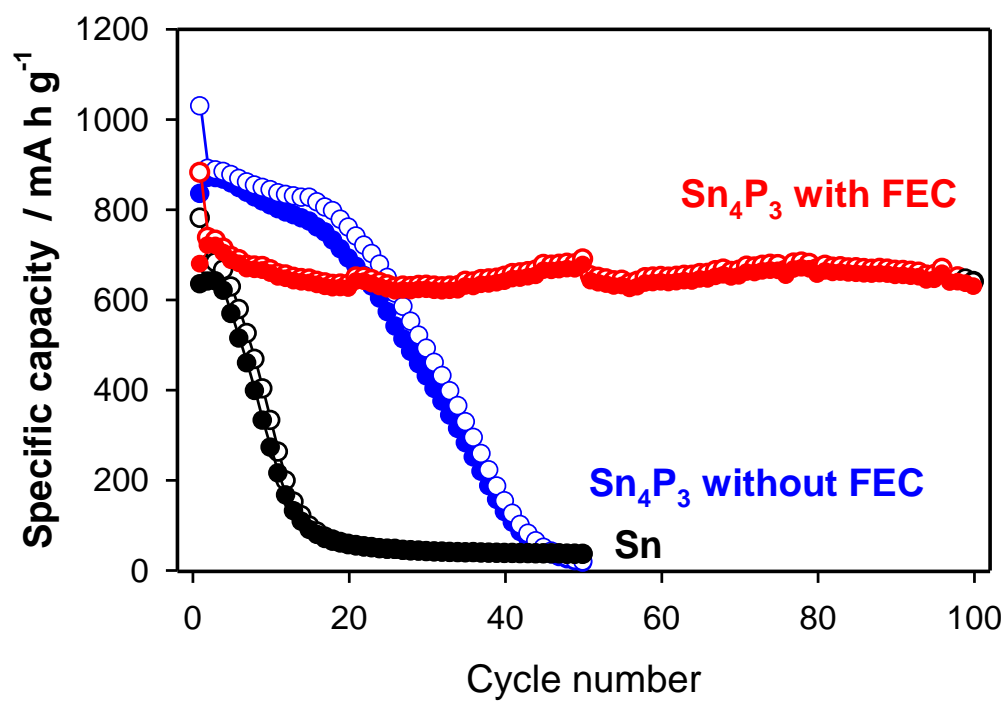
**Figure 31** Cycle performance of $Sn_4P_3$ and Sn electrodes obtained with or without an
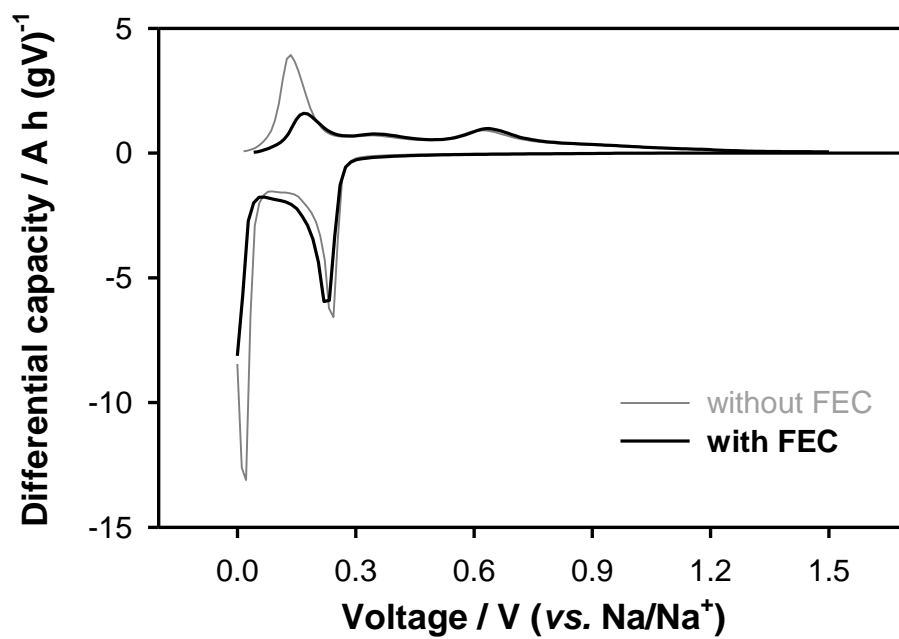
FEC additive.

**Figure 32** Differential capacity (dQ/dV) plots of $Sn_4P_3$ electrodes for the first cycle with or without an FEC additive.
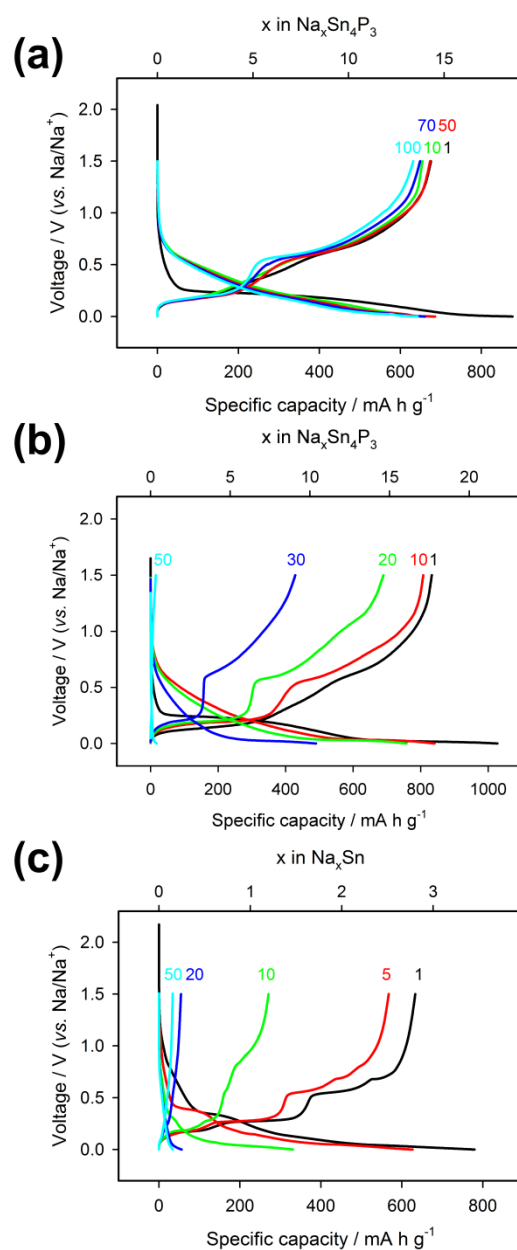
**Figure 33** Voltage profiles of (a) $Sn_4P_3$ with an FEC additive and (b) $Sn_4P_3$ without an FEC additive (c) Sn electrodes with an FEC additive.
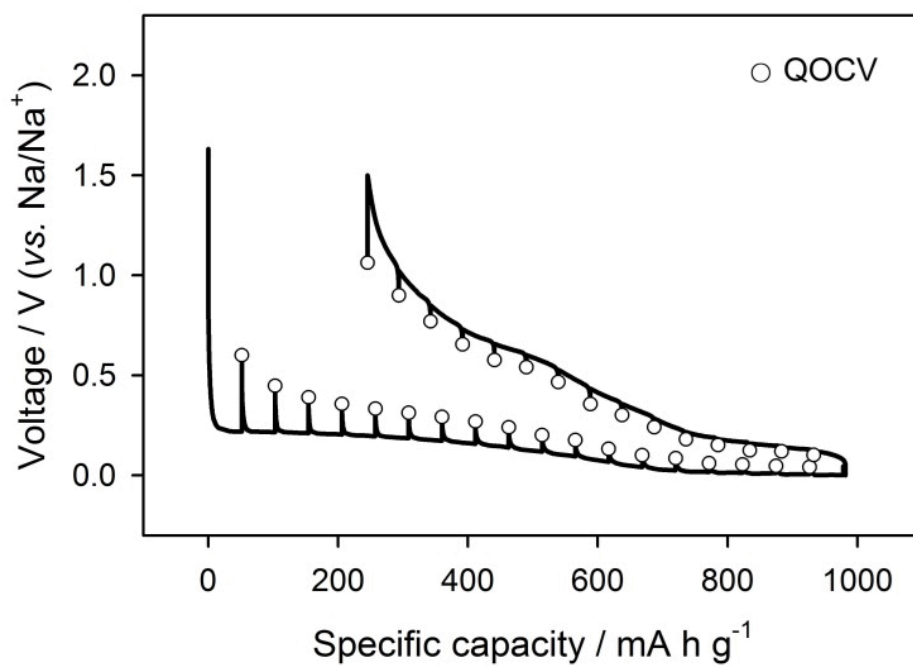
**Figure 34** Quasi-open-circuit-voltage (QOCV) profile of $Sn_4P_3$ obtained via galvanostatic intermittent titration technique.

resistance, causing an increase of polarization and these results in a lower reversible capacity.[45,54,55,63] This is consistent with the differential capacity (dQ/dV) plots of $Sn_4P_3$ with or without the FEC, and $Sn_4P_3$ with the FEC showed smaller polarization than that without the FEC (**Figure 32**). **Figure 33** shows the charge-discharge profiles of the $Sn_4P_3$ with or without the FEC and Sn with the FEC, respectively, between 1.5 and 0 V *vs.* $Na/Na^+$ at a rate of 100 mA $g^{-1}$ (~0.15C). The sodiation profile of $Sn_4P_3$ shows two steps located at ~ 0.2 and 0.01 V *vs.* $Na/Na^+$, which is further supported by differential capacity (dQ/dV) plots (**Figure 32**) and the quasi-open-circuit-voltage (QOCV) profile (**Figure 34**) obtained via the galvanostatic intermittent titration technique. The plateau at *ca.* 0.2 V was attributed to the formation of $Na_xP$ and NaSn phases via a conversion reaction, and further sodiation occured at *ca.* 0.01 V to form $Na_{15}Sn_4$. This sodiation mechanism was supported by *ex- situ* HR-TEM analysis and fast Fourier transformation (FFT) studies. **Figure 35a** and **35b** show the voltage profile of the $Sn_4P_3$ without the FEC and the corresponding HR-TEM images with FFTs (inset: right) of the selected area (inset: left) at various degrees of sodiation, respectively. The initial state before sodiation is $Sn_4P_3$, which is consistent with that the d-spacings obtained from FFT analysis corresponded to (110) and (107) of $Sn_4P_3$ (**Figure 35b (i)**). This is further supported by the selected area electron diffraction (SAED) pattern of the
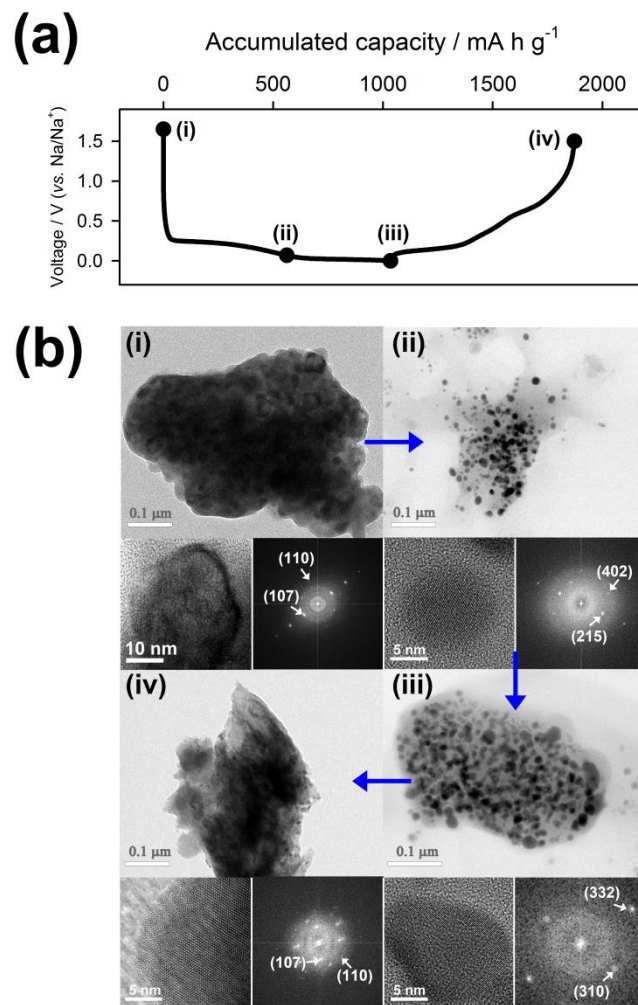
**Figure 35** (a) First galvanostatic charge and discharge profiles of the $Sn_4P_3$ electrode obtained without an FEC additive. The different points indicate (i)pristine, (ii) 0.07 V, (iii) 0 V and (iv) 1.5 V. (b) The ex situ HR-TEM bright-field images at each point in (a) (insets of (i) through (iv): enlarged HR-TEM images (left) of crystalline regions and the corresponding FFT patterns (right)).
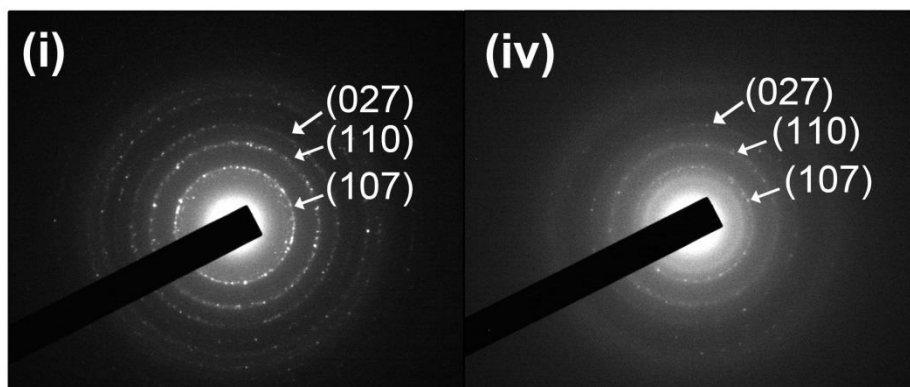
**Figure 36** Electron diffraction (ED) patterns at the points (i) and (iv) in figure 33(a).
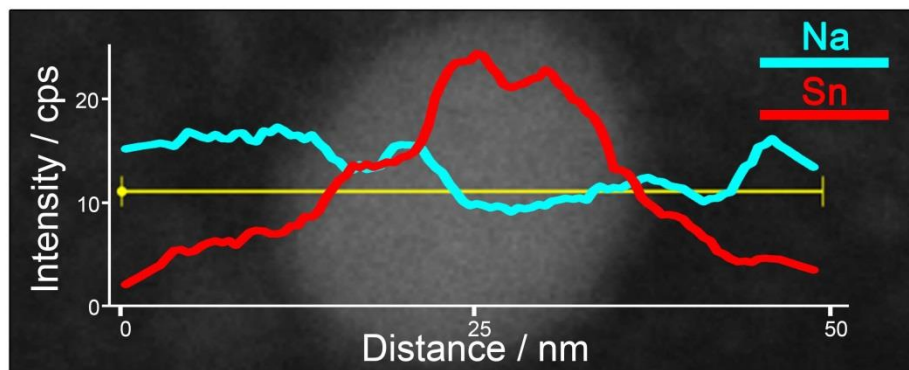
**Figure 37** STEM dark-fi eld image and EDX line profi les of Sn and Na in the nanocrystalline region at the point (ii) in figure 33(a).
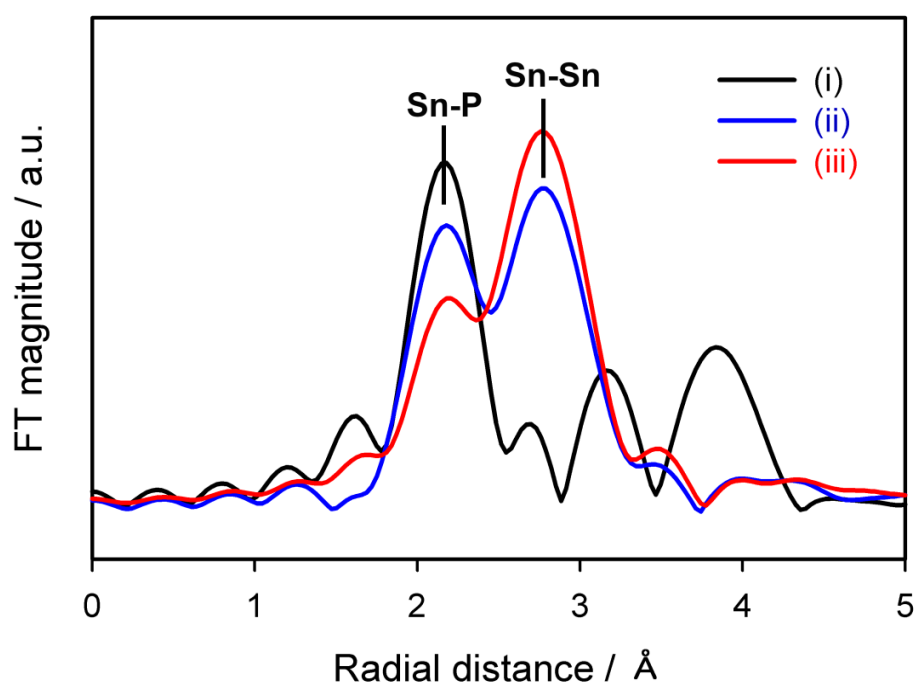
**Figure 38** Sn K-edge EXAFS spectra of $Sn_4P_3$ during sodiation.

initial state, as shown in **Figure 36 (i)**. As the redox potential reached at 0.07 V

*vs.* Na/Na$^+$, NaSn nanocrystallites (dark region) with sizes of tens of

nanometers dispersed in an amorphous Na$_x$P matrix (bright region) were

observed. As shown in the insets of **Figure 35b (ii)**, the d-spacings of the

crystalline nano-domains dispersed in the amorphous matrix measured from

FFT analysis corresponded to (402) and (215) of NaSn. This reveals that NaSn

was formed via the conversion reaction accompanying the formation of

amorphous Na$_x$P. The formation of NaSn nanocrystallites was further supported

by energy dispersive X-ray spectroscopy (EDS) line profiles shown in **Figure

37**. The intensity of Sn increased in the nanocrystalline (bright) region, and the

intensity of Na in the nanocrystalline region was similar to that in the

amorphous (dark) region corresponding to Na$_x$P. This implies that Na was

inserted not only in the amorphous phosphorus matrix but also in the Sn

nanocrystallites. At point (iii) after full sodiation, larger nanocrystallites

dispersed in the amorphous matrix were observed (**Figure 35b (iii)**). The d-

spacings of the crystalline nano-domains dispersed in the matrix measured from

FFT analysis corresponded to (332) and (310) of Na$_{15}$Sn$_4$, indicating that NaSn

was further sodiated to form Na$_{15}$Sn$_4$ at *ca.* 0.01 V. The larger size of the

nanocrystallites shown in (iii) further supported the formation of Na$_{15}$Sn$_4$ (22.3

± 1.1 nm), because the increase in the nanocrystallite size was attributed to the

volume expansion from NaSn (15.1 ± 0.4 nm). In addition, it was considered that this morphology of the confinement of $Na_ySn$ nanocrystallites in the amorphous $Na_xP$ matrix made a critical contribution toward the better cycle performance of $Sn_4P_3$ than Sn. It is well-known that the pulverization or cracking of Sn is caused by the agglomeration of Sn particles during cyclings in Li-ion batteries, resulting in the degradation of Sn electrodes. However, in the case of $Sn_4P_3$, Sn nanocrystallites are embedded in the phosphorus matrix during cyclings, and thus the agglomeration of Sn is inhibited.

The sodiation mechanism of $Sn_4P_3$ is consistent with extended X-ray absorption fine structure (EXAFS) data shown in **Figure 38**. X-ray absorption spectroscopy (XAS) was carried out on Sn atoms in the active electrode materials to observe the evolution of local structural variations during Na insertion. **Figure 38** displays the Fourier transform $k^3\chi(k)$ radial distribution function of the EXAFS signals for $Sn_4P_3$ at selected degrees of sodiation from (i) to (iii). For the pristine electrode, a distinct peak at 2.178 Å corresponding to the Sn-P bond was observed, while the peak corresponding to the Sn-P bond decreased and a new peak corresponding to the Sn-Sn bond appeared at 0.07V (ii). After full sodiation (iii), FT peaks corresponding to the Sn-P bond is notably decreased, indicating that the Sn-P bond cleaved and long range order
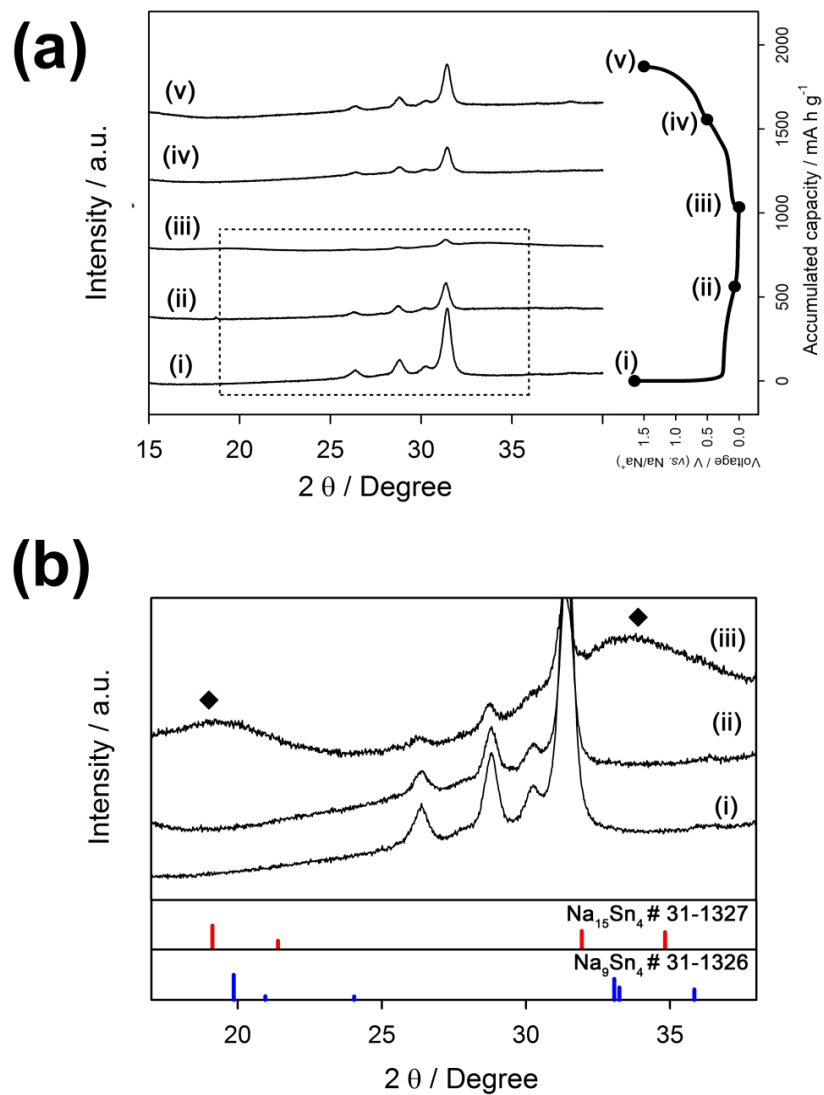
**Figure 39** (a) The *ex-situ* XRD patterns of the Sn$_4$P$_3$ electrode collected at various points as indicated in the corresponding voltage profile: (i) pristine,(ii) 0.07 V, (iii) 0 V, (iv) 0.5 V and (v) 1.5 V. (b) Enlarged *ex-situ* XRD patterns during sodiation.

decreased because of amorphization, as Na ions were inserted in the $Sn_4P_3$ structure.

In order to further clarify the structural changes upon sodiation/desodiation, *ex-situ* XRD analysis of $Sn_4P_3$ was performed, and it revealed that the reversible sodiation/desodiation of $Sn_4P_3$ proceeded in a two-phase reaction, as shown in **Figure 39**. Upon sodiation to 0.07 V, the intensity of XRD peaks corresponding to $Sn_4P_3$ decreased, but no new peaks were observed despite the fact that crystalline NaSn and $Na_{15}Sn_4$ nano-domains were observed in the TEM images. This indicates that an amorphous $Na_xP$ phase was formed during sodiation and nanocrystalline NaSn was not detectable by XRD owing to its very small crystallite size. After full sodiation, very broad peaks corresponding to sodiated Sn phases such as $Na_{15}Sn_4$ and $Na_9Sn_4$ appeared at ~19 and 33$^o$, as shown in the enlarged XRD patterns (**Figure 39b**). This observations agreeed well with the *ex-situ* TEM result (**Figure 35**). On desodiation, the intensity of XRD peaks corresponding to $Sn_4P_3$ gradually increased, indicating that the conversion reaction of $Sn_4P_3$ to $Na_xP$ and $Na_{15}Sn_4$ was reversible. This observation was consistent with the TEM studies of the fully desodiated phase converted from the mixed phases of $Na_xP$ and $Na_{15}Sn_4$, as shown in **Figure 35b** and **c** (iv). The embedded NaSn and $Na_{15}Sn_4$ nanocrystallites in the matrix disappeared after desodiation and formed $Sn_4P_3$. This is supported by that the d-

spacings obtained from FFT analysis corresponded to $Sn_4P_3$ (**Figure 35b** (iv)). Also, this is consistent with the selected area electron diffraction (SAED) pattern after full desodiation corresponding to $Sn_4P_3$, as shown in **Figure 35c** (iv).

**Figure 40** shows a comparison of the voltage profiles of a phosphorus/carbon composite and $Sn_4P_3$. The redox potential of $Sn_4P_3$ is lower than that of phosphorus/carbon composites. This indicates that a full cell with higher energy density can be obtained using a $Sn_4P_3$ anode instead of a phosphorus anode, assuming that equal reversible capacities are utilized. The increase in the redox potential of cathode materials is limited owing to electrolyte decomposition at high potential, and thus it is important to decrease the redox potential of anode materials to increase the working voltage (energy density) of full cells. Therefore, $Sn_4P_3$ is an ideal anode material for Na-ion batteries. The thickness change in electrodes during sodiation and desodiation was measured through ex situ measurements of the electrode thickness (**Figure 40**). The cells were disassembled and the electrode thickness was measured manually at various points indicated in the corresponding voltage profile: (i) pristine, (ii) 0.07 V, (iii) 0 V, (iv) 0.5 V and (v) 1.5 V. After full sodiation until the redox potential of the working electrode reached 0 V *vs.* Na/Na$^+$, the electrode thickness increased by 93%, which is lower than that in the previously
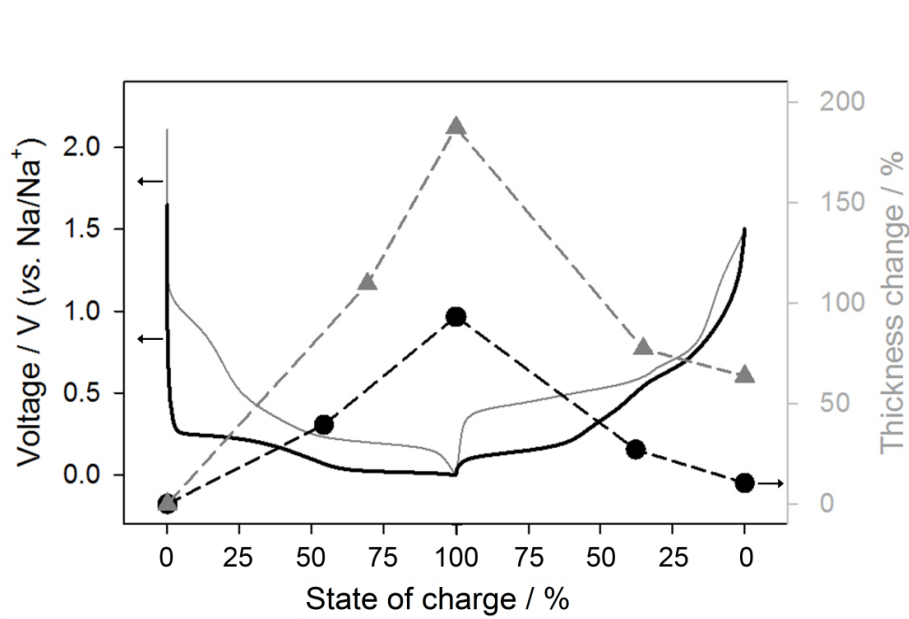
**Figure 40** Voltage profiles of $Sn_4P_3$ (black line) and P/C composite (gray line) and the

corresponding electrode thickness change during sodiation and desodiation

(black circle: $Sn_4P_3$ , gray triangle: P/C).

reported case of the phosphorus/carbon composite (187%). The electrode thickness change during sodiation and desodiation was reversible, and the initial electrode thickness was almost recovered with an expansion of only 11% after full desodiation until the redox potential of the working electrode reached 1.5 V *vs.* Na/Na$^+$. The large volume change in Sn$_4$P$_3$ is a practical obstacle for its commercialization, because the maximum acceptable degree of volume change for commercial electrodes is ~30%. Therefore, it is required to consider new approaches to alleviate cell deformation, including control of electrode porosity and the use of functional binders.

# 5. Conclusions

In this work, application of phosphorus-based high capacity negative electrode materials for sodium-ion battery was investigated. First, the electrochemical reaction mechanism of P/C carbon composites is suggested. Second, failure mechanism and optimization of P/C composites are carried out. Third, $Sn_4P_3$ is notable as a promising negative electrode materials candidate for Na-ion batteries owing to its volumetric specific capacity. The following points of value are summarized.

(i) An amorphous red phosphorus/graphite composite was obtained through a ball milling process, and we have demonstrated, for the first time, its electrochemical performance as a negative electrode material for Na ion batteries. This material showed excellent electrochemical performance, thus making it a promising candidate for Na ion batteries. This material showed the $1^{st}$ cycle desodiation capacity of 1490 mA h $g^{-1}$, the highest value among reported electrode materials for Na ion batteries; appropriate redox potential of *ca.* 0.4 V *vs*. Na/Na$^+$, which is ideal for anode applications from the view-points of safety and energy density.

(ii) The failure mechanism of phosphorus/carbon composites electrode materials has been identified and the feasible solutions provided. In the

desodiation process, the Na extraction is not fully completed due to an increase in internal resistance owing to contact loss between electrode materials and conducting agents. Also, during isotropic volume expansion and contraction of the electrode materials, the SEI layer is repeatedly formed and deformed under large cyclic stresses. These P/C composites show drastic capacity degradation, it is fully susceptible of improvement through changing phosphorus to carbon ratio and electrolyte additives. The change of P to C ratio helps alleviate the huge volumetric expansion and the FEC additives are formation of stable NaF-like SEI film and minimization of EC reduction for long-term cycles. Also, owing to this facile and simple synthesis of the amorphous red phosphorus/carbon composite, phosphorus-based negative electrode materials will be extensively studied for rechargeable batteries including both Li and Na ion batteries. It is expected that this will provide an opportunity for phosphorus-based materials to be successfully utilized for next generation rechargeable batteries.

(iii) Tin phosphide ($Sn_4P_3$) was obtained through ball milling, and we demonstrated, for the first time, its electrochemical performance as an anode material for Na-ion batteries. $Sn_4P_3$ is notable as a promising anode candidate for Na-ion batteries owing to its volumetric specific capacity, which is the

highest among Na-ion insertion materials reported to date, and good electrical conductivity. $Sn_4P_3$ showed excellent electrochemical performance including a reversible capacity of 718 mA h $g^{-1}$; very stable cycle performance with negligible capacity fading over 100 cycles; and an appropriately low redox potential of about 0.3 V $vs.$ Na/Na$^+$, which is ideal for an anode to achieve full cells with high energy density. The better cycle performance of $Sn_4P_3$ than Sn was attributed to the confinement effect of Sn nanocrystallites in the amorphous phosphorus matrix during cycling. Finally, owing to the simple synthesis and excellent electrochemical performance of the $Sn_4P_3$, it is expected that various phosphide-based anode materials including $Sn_4P_3$ will be extensively studied for Na-ion batteries.

# References

(1) Winter, M.; Besenhard, J. O.; Spahr, M. E.; Novák, P. *Adv. Mater.* **1998**, *10*, 725.

(2) Tarascon, J. M.; Armand, M. *Nature* **2001**, *414*, 359.

(3) Yoo, H. D.; Markevich, E.; Salitra, G.; Sharon, D.; Aurbach, D. *Mater. Today* **2014**, *17*, 110.

(4) Diouf, B.; Pode, R. *Renew. Energ.* **2015**, *76*, 375.

(5) Kim, H.-s.; Yoon, T.; Jang, J.; Mun, J.; Park, H.; Ryu, J. H.; Oh, S. M. *J. Power Sources* **2015**, *283*, 300.

(6) Grosjean, C.; Miranda, P. H.; Perrin, M.; Poggi, P. *Renew. Sust. Energ. Rev.* **2012**, *16*, 1735.

(7) Yoo, H. D.; Shterenberg, I.; Gofer, Y.; Gershinsky, G.; Pour, N.; Aurbach, D. *Energy Environ. Sci.* **2013**, *6*, 2265.

(8) Kim, Y.; Ha, K.-H.; Oh, S. M.; Lee, K. T. *Chem. Eur. J.* **2014**, *20*, 11980.

(9) Ellis, B. L.; Nazar, L. F. *Curr. Opin. Solid State Mater. Sci.* **2012**, *16*, 168.

(10) Kim, D.; Kang, S. H.; Slater, M.; Rood, S.; Vaughey, J. T.; Karan, N.; Balasubramanian, M.; Johnson, C. S. *Adv. Energy Mater.* **2011**, *1*, 333.

(11) Kim, S. W.; Seo, D. H.; Ma, X. H.; Ceder, G.; Kang, K. *Adv. Energy Mater.* **2012**, *2*, 710.

(12) Hong, S. Y.; Kim, Y.; Park, Y.; Choi, A.; Choi, N. S.; Lee, K. T. *Energy Environ. Sci.* **2013**, *6*, 2067.

(13) Palomares, V.; Casas-Cabanas, M.; Castillo-Martinez, E.; Han, M. H.; Rojo, T. *Energy Environ. Sci.* **2013**, *6*, 2312.

(14) Pan, H.; Hu, Y.-S.; Chen, L. *Energy Environ. Sci.* **2013**, *6*, 2338.

(15) Slater, M. D.; Kim, D.; Lee, E.; Johnson, C. S. *Adv. Funct. Mater.* **2013**, *23*, 947.

(16) Jache, B.; Adelhelm, P. *Angew. Chem., Int. Ed.* **2014**, *53*, 10169.

(17) Kim, H.; Hong, J.; Park, Y.-U.; Kim, J.; Hwang, I.; Kang, K. *Adv. Funct. Mater.* **2015**, *25*, 534.

(18) Ponrouch, A.; Goñi, A. R.; Palacín, M. R. *Electrochem. Commun.* **2013**, *27*, 85.

(19) Stevens, D. A.; Dahn, J. R. *J. Electrochem. Soc.* **2000**, *147*, 1271.

(20) Komaba, S.; Murata, W.; Ishikawa, T.; Yabuuchi, N.; Ozeki, T.; Nakayama, T.; Ogata, A.; Gotoh, K.; Fujiwara, K. *Adv. Funct. Mater.* **2011**, *21*, 3859.

(21) Chevrier, V. L.; Ceder, G. *J. Electrochem. Soc.* **2011**, *158*, A1011.

(22) Poizot, P.; Laruelle, S.; Grugeon, S.; Dupont, L.; Tarascon, J. M. *Nature* **2000**, *407*, 496.

(23) Bruce, P. G.; Scrosati, B.; Tarascon, J.-M. *Angew. Chem., Int. Ed.* **2008**, *47*, 2930.

(24) Ellis, B. L.; Lee, K. T.; Nazar, L. F. *Chem. Mater.* **2010**, *22*, 691.

(25) Park, Y.; Shin, D.-S.; Woo, S. H.; Choi, N. S.; Shin, K. H.; Oh, S. M.; Lee, K. T.; Hong, S. Y. *Adv. Mater.* **2012**, *24*, 3562.

(26) Cao, Y.; Xiao, L.; Sushko, M. L.; Wang, W.; Schwenzer, B.; Xiao, J.; Nie, Z.; Saraf, L. V.; Yang, Z.; Liu, J. *Nano Lett.* **2012**, *12*, 3783.

(27) Xiong, H.; Slater, M. D.; Balasubramanian, M.; Johnson, C. S.; Rajh, T. *J. Phys. Chem. Lett.* **2011**, *2*, 2560.

(28) Senguttuvan, P.; Rousse, G. l.; Seznec, V.; Tarascon, J.-M.; Palacín, M. R. *Chem. Mater.* **2011**, *23*, 4109.

(29) Park, S. I.; Gocheva, I.; Okada, S.; Yamaki, J.-i. *J. Electrochem. Soc.* **2011**, *158*, A1067.

(30) Xu, Y.; Zhu, Y.; Liu, Y.; Wang, C. *Adv. Energy Mater.* **2013**, *3*, 128.

(31) Xiao, L.; Cao, Y.; Xiao, J.; Wang, W.; Kovarik, L.; Nie, Z.; Liu, J. *Chem. Commun.* **2012**, *48*, 3321.

(32) Qian, J.; Chen, Y.; Wu, L.; Cao, Y.; Ai, X.; Yang, H. *Chem. Commun.* **2012**, *48*, 7070.

(33) Park, C. M.; Sohn, H. J. *Adv. Mater.* **2007**, *19*, 2465.

(34) Qian, J.; Qiao, D.; Ai, X.; Cao, Y.; Yang, H. *Chem. Commun.* **2012**, *48*, 8931.

(35) Marino, C.; Boulet, L.; Gaveau, P.; Fraisse, B.; Monconduit, L. *J. Mater.*

*Chem.* **2012**, *22*, 22713.

(36) Sun, L. Q.; Li, M. J.; Sun, K.; Yu, S. H.; Wang, R. S.; Xie, H. M. *J. Phys. Chem. C* **2012**, *116*, 14772.

(37) Wang, L.; He, X.; Li, J.; Sun, W.; Gao, J.; Guo, J.; Jiang, C. *Angew. Chem., Int. Ed.* **2012**, *51*, 9034.

(38) Marino, C.; Debenedetti, A.; Fraisse, B.; Favier, F.; Monconduit, L. *Electrochem. Commun.* **2011**, *13*, 346.

(39) Mortazavi, M.; Ye, Q.; Birbilis, N.; Medhekar, N. V. *J. Power Sources* **2015**, *285*, 29.

(40) Dahn, J. R. *Phys. Rev. B* **1991**, *44*, 9170.

(41) Extance, P.; Elliott, S. R. *Philos. Mag. B* **1981**, *43*, 469.

(42) Olego, D. J.; Baumann, J. A.; Kuck, M. A.; Schachter, R.; Michel, C. G.; Raccah, P. M. *Solid State Commun.* **1984**, *52*, 311.

(43) van der Pauw, L. J. *Philips Res.Rep* **1958**, *13*.

(44) Darwiche, A.; Marino, C.; Sougrati, M. T.; Fraisse, B.; Stievano, L.; Monconduit, L. *J. Am. Chem. Soc.* **2012**, *134*, 20805.

(45) Kim, Y.; Kim, Y.; Choi, A.; Woo, S.; Mok, D.; Choi, N.-S.; Jung, Y. S.; Ryu, J. H.; Oh, S. M.; Lee, K. T. *Adv. Mater.* **2014**, *26*, 4139.

(46) Ryu, J. H.; Kim, J. W.; Sung, Y.-E.; Oh, S. M. *Electrochem. Solid-State Lett.* **2004**, *7*, A306.

(47) Lee, J. G.; Kim, J.; Park, H.; Lee, J. B.; Ryu, J. H.; Kim, J. J.; Oh, S. M. *J. Electrochem. Soc.* **2015**, *162*, A1579.

(48) Yoon, T.; Nguyen, C. C.; Seo, D. M.; Lucht, B. L. *J. Electrochem. Soc.* **2015**, *162*, A2325.

(49) Choi, N.-S.; Yew, K. H.; Lee, K. Y.; Sung, M.; Kim, H.; Kim, S.-S. *J. Power Sources* **2006**, *161*, 1254.

(50) Etacheri, V.; Haik, O.; Goffer, Y.; Roberts, G. A.; Stefan, I. C.; Fasching, R.; Aurbach, D. *Langmuir* **2012**, *28*, 965.

(51) Nguyen, C. C.; Lucht, B. L. *J. Electrochem. Soc.* **2014**, *161*, A1933.

(52) Komaba, S.; Ishikawa, T.; Yabuuchi, N.; Murata, W.; Ito, A.; Ohsawa, Y. *ACS Appl. Mater. Interfaces* **2011**, *3*, 4165.

(53) Baggetto, L.; Ganesh, P.; Sun, C.-N.; Meisner, R. A.; Zawodzinski, T. A.; Veith, G. M. *J. Mater. Chem. A* **2013**, *1*, 7985.

(54) Ji, L.; Gu, M.; Shao, Y.; Li, X.; Engelhard, M. H.; Arey, B. W.; Wang, W.; Nie, Z.; Xiao, J.; Wang, C.; Zhang, J.-G.; Liu, J. *Adv. Mater.* **2014**, *26*, 2901.

(55) Jang, J. Y.; Lee, Y.-W.; Kim, Y.; Lee, J.; Lee, S.-M.; Lee, K. T.; Choi, N.-S. *J. Mater. Chem. A* **2015**, *3*, 8332.

(56) Seo, D. M.; Chalasani, D.; Parimalam, B. S.; Kadam, R.; Nie, M.; Lucht, B. L. *ECS Electrochem. Lett.* **2014**, *3*, A91.

(57) Li, J.; Li, H.; Wang, Z.; Chen, L.; Huang, X. *J. Power Sources* **2002**, *107*, 1.

(58) Larcher, D.; Tarascon, J. M. *Nat. Chem.* **2015**, *7*, 19.

(59) Kundu, D.; Talaie, E.; Duffort, V.; Nazar, L. F. *Angew. Chem., Int. Ed.* **2015**, *54*, 3431.

(60) Han, M. H.; Gonzalo, E.; Singh, G.; Rojo, T. *Energy Environ. Sci.* **2015**, *8*, 81.

(61) Yabuuchi, N.; Kubota, K.; Dahbi, M.; Komaba, S. *Chem. Rev.* **2014**, *114*, 11636.

(62) Ha , S.; Kim , J.-K.; Choi, A.; Kim, Y.; Lee, K. T. *ChemPhysChem* **2014**, *15*, 1971.

(63) Komaba, S.; Matsuura, Y.; Ishikawa, T.; Yabuuchi, N.; Murata, W.; Kuze, S. *Electrochem. Commun.* **2012**, *21*, 65.

(64) Wang, J. W.; Liu, X. H.; Mao, S. X.; Huang, J. Y. *Nano Lett.* **2012**, *12*, 5897.

(65) Darwiche, A.; Sougrati, M. T.; Fraisse, B.; Stievano, L.; Monconduit, L. *Electrochem. Commun.* **2013**, *32*, 18.

(66) Zhu, H.; Jia, Z.; Chen, Y.; Weadock, N.; Wan, J.; Vaaland, O.; Han, X.; Li, T.; Hu, L. *Nano Lett.* **2013**, *13*, 3093.

(67) Su, D.; Xie, X.; Wang, G. *Chem. Eur. J.* **2014**, *20*, 3192.

(68) Sun, Q.; Ren, Q.-Q.; Li, H.; Fu, Z.-W. *Electrochem. Commun.* **2011**, *13*,

1462.

(69) Baggetto, L.; Allcorn, E.; Manthiram, A.; Veith, G. M. *Electrochem. Commun.* **2013**, *27*, 168.

(70) Yu, D. Y.; Prikhodchenko, P. V.; Mason, C. W.; Batabyal, S. K.; Gun, J.; Sladkevich, S.; Medvedev, A. G.; Lev, O. *Nat. Commun.* **2013**, *4*, 2922.

(71) Zhu, Y.; Han, X.; Xu, Y.; Liu, Y.; Zheng, S.; Xu, K.; Hu, L.; Wang, C. *ACS Nano* **2013**, *7*, 6378.

(72) He, M.; Kravchyk, K.; Walter, M.; Kovalenko, M. V. *Nano Lett.* **2014**.

(73) Kim, Y.; Park, Y.; Choi, A.; Choi, N.-S.; Kim, J.; Lee, J.; Ryu, J. H.; Oh, S. M.; Lee, K. T. *Adv. Mater.* **2013**, *25*, 3045.

(74) Li, W.-J.; Chou, S.-L.; Wang, J.-Z.; Liu, H.-K.; Dou, S.-X. *Nano Lett.* **2013**, *13*, 5480.

(75) Qian, J.; Wu, X.; Cao, Y.; Ai, X.; Yang, H. *Angew. Chem., Int. Ed.* **2013**, *52*, 4633.

(76) Yabuuchi, N.; Matsuura, Y.; Ishikawa, T.; Kuze, S.; Son, J.-Y.; Cui, Y.-T.; Oji, H.; Komaba, S. *ChemElectroChem* **2014**.

(77) Zhu, Y.; Wen, Y.; Fan, X.; Gao, T.; Han, F.; Luo, C.; Liou, S.-C.; Wang, C. *ACS Nano* **2015**, *9*, 3254.

(78) Song, J.; Yu, Z.; Gordin, M. L.; Hu, S.; Yi, R.; Tang, D.; Walter, T.; Regula, M.; Choi, D.; Li, X.; Manivannan, A.; Wang, D. *Nano Lett.* **2014**, *14*,

6329.

(79) Yabuuchi, N.; Kajiyama, M.; Iwatate, J.; Nishikawa, H.; Hitomi, S.; Okuyama, R.; Usui, R.; Yamada, Y.; Komaba, S. *Nat. Mater.* **2012**, *11*, 512.

(80) Kim, Y.-U.; Lee, C. K.; Sohn, H.-J.; Kang, T. *J. Electrochem. Soc.* **2004**, *151*, A933.

(81) León, B.; Corredor, J. I.; Tirado, J. L.; Pérez-Vicente, C. *J. Electrochem. Soc.* **2006**, *153*, A1829.

(82) Pralong, V.; Souza, D. C. S.; Leung, K. T.; Nazar, L. F. *Electrochem. Commun.* **2002**, *4*, 516.

(83) Souza, D. C. S.; Pralong, V.; Jacobson, A. J.; Nazar, L. F. *Science* **2002**, *296*, 2012.

(84) Bichat, M. P.; Politova, T.; Pascal, J. L.; Favier, F.; Monconduit, L. *J. Electrochem. Soc.* **2004**, *151*, A2074.

(85) Gillot, F.; Boyanov, S.; Dupont, L.; Doublet, M. L.; Morcrette, M.; Monconduit, L.; Tarascon, J. M. *Chem. Mater.* **2005**, *17*, 6327.

(86) Boyanov, S.; Bernardi, J.; Gillot, F.; Dupont, L.; Womes, M.; Tarascon, J. M.; Monconduit, L.; Doublet, M. L. *Chem. Mater.* **2006**, *18*, 3531.

(87) Kim, Y.; Hwang, H.; Yoon, C. S.; Kim, M. G.; Cho, J. *Adv. Mater.* **2007**, *19*, 92.

(88) Boyanov, S.; Zitoun, D.; Ménétrier, M.; Jumas, J. C.; Womes, M.; Monconduit, L. *J. Phys. Chem. C* **2009**, *113*, 21441.

(89) Lu, Y.; Tu, J.-P.; Xiong, Q.-Q.; Xiang, J.-Y.; Mai, Y.-J.; Zhang, J.; Qiao, Y.-Q.; Wang, X.-L.; Gu, C.-D.; Mao, S. X. *Adv. Funct. Mater.* **2012**, *22*, 3927.

(90) Jang, J. Y.; Park, G.; Lee, S.-M.; Choi, N.-S. *Electrochem. Commun.* **2013**, *35*, 72.

(91) Stan, M. C.; Klöpsch, R.; Bhaskar, A.; Li, J.; Passerini, S.; Winter, M. *Adv. Energy Mater.* **2013**, *3*, 231.

(92) Eckerlin, P.; Kischio, W. *Z. Anorg. Allg. Chem.* **1968**, *363*, 1.

# 요약 (국문초록)

리튬 이온을 기반으로 하는 이차전지 시장은 작게는 휴대폰, 노트북 등의 소형 휴대용 기기의 전력원부터 자동차의 가솔린 엔진을 대체할 동력원에 이르기까지 계속적으로 신규 수요를 창출하며 에너지 저장 분야의 파이를 키워가고 있다. 하지만 매장된 리튬 자원이 일부 지역에 편중되어 있기 때문에 소재 공급 측면에서 가격 인상 요인과 그 매장량의 한계도 고려할 필요가 생겼고, 포스트-리튬 이온 전지 시스템에 대한 많은 연구가 시작하였다. 그 대안으로 고려되고 있는 시스템으로 나트륨 이온 전지가 각광 받고 있다. 나트륨은 리튬에 비해 매장량이 풍부하기 때문에 가격적 측면에서 우세하다. 그러므로 대용량의 전력 저장 시스템(ESS) 시장에서 경쟁력을 가질 것이라 판단된다. 또한 주기율표 상에서 리튬 바로 아래에 위치하는 원소로 화학적 특성이 리튬과 가장 유사하기 때문에 리튬 이온 전지의 반응 기구와 크게 상이하지 않을 것으로 기대한다. 고로 이미 상용화된 리튬 시스템의 대부분을 나트륨 이온 전지로 곧바로 적용 가능할 수가 있기 때문에 진입 장벽도 낮다고 할 수 있다. 하지만 에너지는 용량과 반응 전압의 곱으로 나타내어지는데

양극의 경우, 기존 리튬 이온전지에 비해 나트륨 이온 전지가 가지는 장점이 거의 없다. 따라서 다양한 반응 기구를 적용할 수 있는 음극 활물질의 용량 개선이 중요하다.

본 논문에서는 열역학 정보를 기반으로 하여 나트륨과 상평형을 이루는 적린 (red phosphorus) 을 음극 활물질로 적용 가능성 평가와 이의 전기화학 반응 메커니즘 분석을 하였다. 먼저 적린의 낮은 전기 전도도로 인해 반응 제한 되는 단점을 극복하기 위해 탄소 코팅을 하여 전기화학 반응성 및 가역성을 향상 시켰다. 이를 통해 현재까지 보고된 음극 활물질 중 가장 큰 용량을 발현하는 것을 확인하였다. 전기화학 반응과 결정학 분석을 통해 나트륨이 삽입됨에 따라, 비정질의 적린에서 비정질의 $Na_xP$ 를 거친 뒤 결정질의 $Na_3P$ 가 형성되고 이 반응은 2상 반응 (two-phase reaction) 임을 확인할 수 있었다. 또한 산화과정의 전압 미분 곡선 (dQ/dV) 을 통해, $Na_3P$ 와 관련된 피크가 0.55 V *vs.* $Na/Na^+$ 에서 관찰됨을 알 수 있었다. 하지만 사이클 특성이 매우 좋지 못한데, 이 원인은 충방전 간의 큰 부피 변화가 그 원인이다.

이러한 부피 변화는 전지 퇴화의 원인이 된다. 먼저 충전 시 부피

팽창이 발생하게 되고 이후에 방전 과정에서 수축하게 되면서 활물질과 도전제 혹은 집전체와의 접촉이 손실되면서 전자 전달 경로를 상실할 수 있다. 또한 부피 팽창 시 생성되었던 SEI 가 수축 과정에서 파괴 되고 이 부분에 반복적으로 SEI 생성 및 파괴 현상이 일어나게 된다. 이로 인해 SEI 가 매우 두꺼워져, 입자의 저항을 상승시키는 원인이 된다. 전극의 충방전 도중 부피 변화로 인한 전지 퇴화를 억제 하기 위해 두 가지의 실험을 진행하였다. 먼저 부피 변화를 완화시키기 위해 활물질의 양을 줄이고 카본의 양을 늘렸고, 또한 기계적 강도가 우수한 SEI 형성을 위하여 FEC 첨가제를 사용하였다. 카본의 양을 증가 시킨 경우, 활물질의 양을 감소시켜 절대적인 부피 팽창을 완화시켰고, 전지 내 저항 증가로 인하여 부피 팽창을 감소 시켰다. GP37 전극 물질을 바탕으로 전해질 첨가제인 FEC 를 적용하였을 때, NaF 계열의 피막과 장기 수명에서 EC 분해 반응의 억제로 인하여 100 사이클까지 우수한 수명특성을 관찰할 수 있었다. 하지만 FEC 유무 모두 사이클 도중 입자의 분쇄화로 인해 결정질 $Na_3P$ 상의 형성이 관찰되었으나, FEC 가 첨가되지 않은 전해질의 경우 결정상 생성 후 퇴화가 관찰되고 첨가한 경우 좋은

수명이 관찰되었다. 이는 결정상이 퇴화의 직접적인 원인이 아니고 표면 피막이 그 원인임을 알 수 있었고, 전지 내 비균일한 충방전이 일어나고 있음을 확인할 수 있었다.

마지막으로 최근 여러 시스템에서 한정된 부피 안에서 고용량 발현을 요구하는 경우가 대부분인데, 적린과 탄소 복합체의 경우 밀도가 매우 낮아서 부피당 용량 특성이 매우 떨어진다. 이에 고용량 음극 활물질인 인에 주석의 합금을 형성하여 물리적 특성이 전기 전도도와 밀도를 향상시키고, 주석의 전기화학 반응성 및 가역성을 향상시켰다. 이를 통해 현재까지 보고된 음극 활물질 중 가장 큰 부피당 용량을 발현하는 음극 활물질임을 확인 할 수 있었다.